



## 저작자표시-비영리-변경금지 2.0 대한민국

이용자는 아래의 조건을 따르는 경우에 한하여 자유롭게

- 이 저작물을 복제, 배포, 전송, 전시, 공연 및 방송할 수 있습니다.

다음과 같은 조건을 따라야 합니다:



저작자표시. 귀하는 원저작자를 표시하여야 합니다.



비영리. 귀하는 이 저작물을 영리 목적으로 이용할 수 없습니다.



변경금지. 귀하는 이 저작물을 개작, 변형 또는 가공할 수 없습니다.

- 귀하는, 이 저작물의 재이용이나 배포의 경우, 이 저작물에 적용된 이용허락조건을 명확하게 나타내어야 합니다.
- 저작권자로부터 별도의 허가를 받으면 이러한 조건들은 적용되지 않습니다.

저작권법에 따른 이용자의 권리는 위의 내용에 의하여 영향을 받지 않습니다.

이것은 [이용허락규약\(Legal Code\)](#)을 이해하기 쉽게 요약한 것입니다.

[Disclaimer](#)

2019年 8月

2019 年 8 月  
博士學位論文

博士學位論文

Surface characteristics of (Mg/Si)-hydroxyapatite coated Ti-29Nb-xHf alloys by plasma electrolyte oxidation for dental implant

# Surface characteristics of (Mg/Si)-hydroxyapatite coated Ti-29Nb-xHf alloys by plasma electrolyte oxidation for dental implant

朝鮮大學校 大學院

齒醫學科

朴 宣 映

朴  
宣  
映

# Surface characteristics of (Mg/Si)-hydroxyapatite coated Ti-29Nb-xHf alloys by plasma electrolyte oxidation for dental implant

플라즈마 전해 산화법으로  
(Mg/Si)-hydroxyapatite 코팅된 치과 임플란트용  
Ti-29Nb-xHf 합금의 표면특성

2019 年 8 月 23 日

朝鮮大學校 大學院

齒醫學科

朴 宣 映

# Surface characteristics of (Mg/Si)-hydroxyapatite coated Ti-29Nb-xHf alloys by plasma electrolyte oxidation for dental implant

指導教授 崔 漢 喆

이 論文을 齒醫學 博士學位申請 論文으로 提出함






2019 年 4 月

朝鮮大學校 大學院

齒醫學科

朴 宣 映

## 朴宣映의 博士學位論文을 認准함

委 員 長	朝鮮大學校	教 授	鄭 在 憲	
委 員	全南大學校	教 授	朴 相 元	
委 員	光州女子大學校	教 授	文 相 銀	
委 員	朝鮮大學校	教 授	孫 美 敬	
委 員	朝鮮大學校	教 授	崔 漢 喆	

2019 年 6 月

朝鮮大學校 大學院

## Contents

LIST OF TABLES .....	III
LIST OF FIGURES .....	V
ABSTRACTS .....	VIII
 I . General Introduction .....	 1
 II . Background .....	 3
2.1. Titanium .....	3
2.2. Titanium properties .....	6
2.2.1. Ti-Nb-Hf system .....	7
2.3. Titanium oxide surface .....	11
2.4. Electrochemical anodization process .....	14
2.5. Micro-porous oxide formation .....	16
2.6. Effect of magnesium (Mg) and silicon (Si) in the bone .....	18
 III . Materials and Method .....	 22
3.1. The preparation of Ti-29Nb-xHf alloys .....	22
3.2. The characterization of Ti-29Nb-Hf alloys .....	23
3.3. Micro-pore formation on the alloy surface .....	24
3.4. Measurement of mechanical properties .....	27
3.5. Surface wettability measurement .....	28
3.6. Electrochemical tests .....	30
3.7. Formation of bone-like apatite in simulated body fluid .....	31

3.8. MC3T3-E1 cell culture test	33
<b>IV. Results and Discussion</b>	34
4.1 Microstructure observation of Ti-29Nb-xHf alloys	34
4.2 Corrosion behavior of Ti-29Nb-xHf alloys	39
4.3 Mechanical properties of Ti-29Nb-xHf alloys	46
4.4 Micro-pore formation on the alloy surface	51
4.5 Electrochemical behaviors of Ti-29Nb and Ti-29Nb-15Hf alloys	62
4.6 Biocompatibility of Ti-29Nb and Ti-29Nb-15Hf alloys	66
<b>V. Conclusions</b>	74
<b>Reference</b>	76

## LIST OF TABLES

Table 1. Mechanical properties of selected implant metals .....	4
Table 2. Summarized properties of biomaterials.....	5
Table 3. Physical property of titanium.....	10
Table 4. Physical properties and crystal structure of $TiO_2$ .....	12
Table 5. physicochemical properties of titanium oxide and other metal oxides.....	13
Table 6. Effect of selected metallic ions on human bone metabolism and angiogenesis : summary of literature studies.....	20
Table 7. Comparative composition of human enamel, dentin, and bone.....	21
Table 8. The condition of different electrolytes containing plasma electrolytic oxidation.....	25
Table 9. The condition of plasma electrolytic oxidation.....	26
Table 10. Composition of SBF, in comparison with human blood plasma.....	32
Table 11. Electrochemical parameters of non-treated Ti-29Nb-xHf alloys from potentiodynamic polarization test .....	43
Table 12. Vicker' s hardness values of Ti-29Nb-xHf alloy.: (a) Ti-29Nb, (b) Ti-29Nb-3Hf, (c) Ti-29Nb-7Hf, and (d) Ti-29Nb-15Hf .....	50
Table 13. The summarized data from image analysis for the micro-pore formed on Ti-29Nb and Ti-29Nb-15Hf alloys by PEO.....	57
Table 14. EDS mapping result of Ti-29Nb and Ti-29Nb-15Hf alloys with different electrolytes containing Mg concentration.....	59
Table 15. Electrochemical parameters of PEO-treated Ti-29Nb and Ti-29Nb-15Hf alloys with concentration of Mg ion from anodic polarization curves: corrosion potential( $E_{corr}$ ), corrosion current density( $I_{corr}$ ), current density at 300 mV( $I_{300mV}$ ),	



and primary passivation current density( $I_{pp}$ )..... 65

## LIST OF FIGURES

Fig. 1. Allotropic transformation of titanium.....	8
Fig. 2. Phase diagram of Ti and $\beta$ -stabilization concentration.....	9
Fig. 3. Schematic diagram of electrode processes in electrolysis of aqueous solutions.....	15
Fig. 4. Equilibrium wetting state of liquid.....	29
Fig. 5. OM images of Ti-29Nb-xHf alloys after heat treatment at 1050°C for 12hrs in Ar atmosphere, followed by 0°C water quenching: (a) Ti-29Nb, (b)Ti-29Nb-3Hf, (c) Ti-29Nb-7Hf, and (d) Ti-29Nb-15Hf.....	36
Fig. 6. XRF results of Ti-29Nb-xHf alloys after heat treatment at 1050°C for 12hrs in Ar atmosphere, followed by 0°C water quenching: (a) Ti-29Nb, (b)Ti-29Nb-3Hf, (c) Ti-29Nb-7Hf, and (d) Ti-29Nb-15Hf.....	37
Fig. 7. XRD results of Ti-29Nb-XHf alloys after heat treatment at 1050°C for 12hrs in Ar atmosphere, followed by 0°C water quenching: (a) Ti-29Nb, (b)Ti-29Nb-3Hf, (c) Ti-29Nb-7Hf, and (d) Ti-29Nb-15Hf.....	38
Fig. 8. Anodic polarization curves of Ti-29Nb-xHf alloys after potentiodynamic test in 0.9% NaCl solution at $36.5 \pm 1^\circ \text{C}$ .....	41
Fig. 9. Bode-plots and Bode-phase for Ti-259Nb-xHf alloys after AC impedance test in 0.9% NaCl solution at $36.5 \pm 1^\circ \text{C}$ : (a) Bode-plots and (b) Bode-phase plots. ....	42
Fig. 10. Equivalent circuit of bulk Ti-29Nb-xHf alloys with anodic oxide layer. ....	44
Fig. 11. Corrosion morphologies of Ti-29Nb-xHf alloys after potentiodynamic test in 0.9% NaCl solution at $36.5 \pm 1^\circ \text{C}$ : (a) Ti-29Nb, (b) Ti-29Nb-3Hf, (c) Ti-29Nb-7Hf, and	

(d) Ti-29Nb-15Hf.....	45
Fig. 12. Vicker' s hardness graph of Ti-29Nb-xHf alloys: (a) Ti-29Nb, (b) Ti-29Nb-3Hf, (c) Ti-29Nb-7Hf, and (d) Ti-29Nb-15Hf.....	48
Fig. 13. Nano-indentation test results of Ti-29Nb-xHf alloys.....	49
Fig. 14. FE-SEM images showing morphologies of PEO-treated Ti-29Nb alloy: (a) low-magnification (x 5,000) and (b) high-magnification (x 50,000).....	54
Fig. 15. FE-SEM images showing morphologies of PEO treated Ti-29Nb alloy (a,b,c, and d) and Ti-29Nb-15Hf alloy (a-1, b-1, c-1, and d-1) with different electrolytes containing Mg concentration of (a and a-1) 0 Mg (b and b-1) 5 Mg, (c and c-1) 10 Mg, and (d and d-1) 20 Mg.....	55
Fig. 16. FE-SEM and pore distribution images of micro-pore formed Ti-29Nb alloy(a,b,c, and d) and Ti-29Nb-15Hf alloy(a-1, b-1, c-1, and d-1) by PEO processing with different electrolytes containing Mg concentration of (a and a-1) 0 Mg, (b and b-1) 5 Mg, (c and c-1) 10 Mg, and (d and d-1) 20 Mg.....	56
Fig. 17. EDS mapping analysis results of PEO-treated (a) Ti-29Nb and (b) Ti-29Nb-15Hf. ....	58
Fig. 18. Variation of Ca/P molar ratio with different electrolytes containing Mg concentration: (a) Ca/P ratio and (b) (Ca+Mg/P+Si) ratio.....	60
Fig. 19. TF-XRD patterns of PEO-treated Ti-29Nb and Ti-29Nb-15Hf alloys with different electrolytes containing Mg concentration of (a) 0Mg, (b) 5Mg, (c) 10Mg, and (d) 20Mg.....	61
Fig. 20. Anodic polarization curves of PEO-treated Ti-29Nb-xHf alloys after potentiodynamic test in 0.9% NaCl solution at $36.5 \pm 1^\circ\text{C}$ : (a) Ti-29Nb and (b) Ti-29Nb-15Hf.....	64
Fig. 21. Contact angles of Ti-29Nb and Ti-29Nb-15Hf	

alloy surfaces: (a and a-1) 0 Mg, (b and b-1) 5 Mg, (c and c-1) 10 Mg, and (d and d-1) 20 Mg.....	69
Fig. 22. FE-SEM images showing morphology of bone-like apatite: (a) low-magnification (x 5,000) and (b) high-magnification (x 50,000). ....	70
Fig. 23. FE-SEM images showing morphology of bone-like apatite: Ti-29Nb alloy: (a) 0 Mg, (b) 5 Mg, (c) 10 Mg, and (d) 20 Mg, and Ti-29Nb-15Hf alloy: (a-1) 0 Mg, (b-1) 5 Mg, (c-1) 10 Mg, and (d-1) 20 Mg.....	71
Fig. 24. FE-SEM images showing morphology of cell cultured Ti-29Nb-15Hf alloy: (a) low-magnification (x 1,000), middle-magnification (x 3,000), and (b) high-magnification (x 10,000).....	72
Fig. 25. FE-SEM images showing morphology of cell cultured Ti-29Nb-xHf alloys for 1day: Ti-29Nb alloy: (a) 0 Mg, (b) 5 Mg, (c) 10 Mg, and (d) 20 Mg, and Ti-29Nb-15Hf alloy: (a-1) 0 Mg, (b-1) 5 Mg, (c-1) 10 Mg, and (d-1) 20 Mg.....	73

## 국 문 초 록

### 플라즈마 전해 산화법으로 (Mg/Si)-hydroxyapatite 코팅된 치과 임플란트용 Ti-29Nb-xHf 합금의 표면특성

박 선 영

지도교수: 최한철, 공학/치의학박사

치의학과

조선대학교 대학원

본 논문에서는 Ti-29Nb-xHf 합금표면에 (Mg/Si)-hydroxyapatite 함유된 마이크로 포어 산화막을 형성하기 위하여 플라즈마 전해 산화법(PEO)으로 합금표면에 포어를 형성하여 표면특성을 연구하였다. 이를 위하여 Ti-29Nb-xHf 이원계, 삼원계 합금은 아크용해법을 이용하여 Ti-29Nb, Ti-29Nb-3Hf, Ti-29Nb-7Hf, 및 Ti-29Nb-15Hf 합금이 되도록 설계하여 제조하였다. 제조된 합금은 디스크형태로 두께 3mm로 절삭하여 1050°C에서 12시간동안 열처리 후 급속 냉각 과정을 걸쳐 시편을 준비하였다. 플라즈마 전해 산화법을 이용하여 Mg, Si 이온이 함유된 Calcium acetate와 Calcium glycerophosphate 전해질 용액에서 표면에 마이크로 포어를 형성하였다. 모든 시편의 표면은 OM, FE-SEM, XRF 및 XRD 등으로 분석하였다. 표면의 경도와 탄성계수는 나노인덴터를 이용하여 조사하였으며 동전위 분극 시험을 통해 표면의 전기화학적 부식 거동을 분석하였고, In vitro 분석은 표면 조건에 대한 생물학적 변화의 영향을 조사하기 위하여 MC3T3 세포로 수행하여 다음과 같은 결과를 얻었다.

1. Ti-29Nb, Ti-29Nb-3Hf, 및 Ti-29Nb-7Hf에서 주로 층상(lamellar)과 침상(needle)형상의 마르텐사이트(martensitic) 구조를 보였으며  $\alpha''$  상이 관찰되었고, Ti-29Nb-15Hf 합금에서는 주로 등축정(equiaxed) 구조로  $\beta$  상이 관찰되었다.

2. 기계적 특성의 분석 결과, Ti-29Nb 합금과 비교하여 Ti-29Nb-3Hf, Ti-29Nb-7Hf, 및 Ti-29Nb-15Hf 순으로 Hf 함량이 증가함에 따라 탄성계수와 경도가 감소하였다.
3. 각 군마다 다양한 직경의 기공들이 산화막 표면에 균일하게 분포되어 있으며, 인가전압이 동일한 환경에서 Mg 이온의 함량이 높아질수록 직경의 크기는 작아지고 균일한 기공이 형성되었으며 Ti-29Nb 이원계와 Ti-29Nb-15Hf 삼원계 합금에서 비슷한 포아 형태와 분포도를 보였다.
4. EDS와 Mapping을 통한 분석 결과, 플라즈마 전해 산화법을 이용하여 처리한 산화막 표면에서 Ca, P, Si, 및 Mg 원소들이 잘 분포되었음을 확인하였다. 특히, Ca/P 및 (Ca+Mg)/(Si+P)비율이 Mg의 함량이 증가할수록 감소하였으며 5 mol%의 Mg에서 이상적인 비율을 나타냈다.
5. XRD 분석 결과, 전해질에 Mg 이온을 첨가한 경우 Ti-29Nb-xHf 합금에서 아나타제 피크가 더 낮은 회절각에서 나타났으며 Mg이 첨가되지 않은 것에 비해 왼쪽으로 shift 하였다.
6. PEO법을 이용하여 표면처리한 Ti-29Nb-xHf합금의  $E_{corr}$ 는 Mg 이온이 증가함에 따라 증가하였고, Ti-29Nb-15Hf 합금은 Ti-29Nb 합금의  $E_{corr}$ 보다 높게 나타났다.
7. 표면처리한 후 젖음성 분석한 결과, Mg 이온의 함량을 증가시킴에 따라 표면에서 낮은 접촉각이 나타났다. 또한, Ti-29Nb 보다 Ti-29Nb-15Hf에서 더 낮은 접촉각을 보였다.
8. In vitro 분석 결과, PEO 처리된 표면에서 전체적으로 안정적인 골성장과 세포 성장을 보였다. 특히, 5 mol%의 Mg에서 골성장과 세포의 성장이 가장 우수하였다.

결론적으로, 합금의 낮은 탄성계수와 (Mg/Si)-hydroxyapatite가 함유된 마이크로 포어 산화막이 형성된 Ti-29Nb-xHf 합금은 골형성을 유도할 수 있는 세포부착과 성장의 친화적인 환경을 제공할 것으로 생각되며 생체재료로서 응용이 가능함을 알 수 있었다.

## I . INTRODUCTION

Commercial pure titanium (CP-Ti) and titanium (Ti) alloys have been used as an implant material from orthopedics and dental field. Because, its alloys have low elastic modulus, mechanical properties, good corrosion resistance and excellent biocompatibility [1-5]. However, CP-Ti and Ti alloys have some problems such as high modulus of elasticity and toxic. Especially, Ti-6Al-4V alloy has toxic elements such as Alzheimer's disease of Al element and toxicity of V element, it can create harmful environment [6-8]. So, some researchers have been studies on problems of Ti alloys. They have focused on nontoxic element such as niobium (Nb), hafnium (Hf), tantalum (Ta), and zirconium (Zr) for controlling the contents. Especially, Nb and Hf element are effective titanium  $\beta$ -stabilizers and complete mutual solubility in Ti phases [11-15]. Therefore, Nb and Hf element will have superior properties of alloys and biocompatibility such as the Ti-Nb-Hf alloy.

Many researchers have been studies various surface modifications of Ti alloys to improve their bioactivity due to insufficient adhesion of cells on bulk Ti surface. The plasma electrolytic oxidation (PEO) is one of various process, it can occur very quickly to anodic spark oxidation from  $TiO_2$  again. Micro-arc oxidation and anodic spark oxidation are created based on PEO process. The micro-arc oxidation shows many advantages, such as adhesion of substrate metal, corrosion of Ti alloy and biocompatibility of Ti alloy surfaces to improve a surface property [13-20]. From previous reports, anodized  $TiO_2$  surface provided higher cell adhesion, proliferation, and cells cultured on anodized  $TiO_2$  surfaces, it leads to higher ALP activity, compared with the control surface such as a physical change [21, 22]. Especially, PEO process can control electrolyte composition, applied voltage, current density and applied time, which can incorporate Ca and P ions on the  $TiO_2$  surface [23-25]. PEO process for active surface can be carried out in electrolytes containing Ca and P ions or other ions. Natural

bone is composed of mineral elements such as magnesium (Mg), silicon (Si), zinc (Zn), strontium (Sr), and manganese (Mn), etc. Especially, Mg is closely related to indirectly affect mineral metabolism and calcification of bone tissue. Also, role of Si deficiency has been reported to affect bone formation and growth after clinical implantation of bio-implants [25-27]. However, there were a little researches focused on PEO-treated Ti alloy in electrolyte containing Ca, P, Mg, and Si ions for improvement of biocompatibility.

In this study, the surface characteristics of (Mg/Si)-hydroxyapatite coated Ti-29Nb-xHf alloys by plasma electrolyte oxidation for dental implant have researched using various experimental instruments.



## II . BACKGROUND

### 2.1. Titanium[20-27]

Dental materials have been used successfully for a variety of biocompatible materials and other applications. CP Ti (commercial pure titanium), Ti-6Al-4V and nickel-titanium shape memory alloys are widely used due to several advantages, including low elastic modulus, excellent corrosion resistance and improved biocompatibility as shown in Table 1. [21-23]. Metal materials used for long periods of time in orthopedic and dental areas should be free of toxic or allergic reactions to patients or manipulators and should not cause changes in the corrosion or physical properties of the equipment in the environment. Table 1 summarizes the mechanical properties of various implant metal materials specified by the ASTM standard [24]. However, in the case of the Ti-6Al-4V alloy widely used, there are some disadvantages such as the release of the elements Al and V which are cytotoxic to the human body, and these elements may have an undesirable negative effect [25,26]. Principal requirements for all the biomaterials, including metalics, are presently understood to be: corrosion resistance, biocompatibility, bioadhesion (bone ingrowth), mechanical properties, availability. The characteristics of the implants when selecting or developing bio alloys are shown in Table 2. When a metal implant is implanted in a living body, biomolecules such as biological fluids including various cells and water, dissolved ions, and proteins surrounded by water molecules are adhered to determine the affinity of the alloy by the biological reaction with the metal material[25-27].



Table 2. Summarized properties of biomaterials[26]

Biomaterials	Mechanical Properties
<ul style="list-style-type: none"> <li>- Osseointegration</li> <li>- Bio corrosion resistance</li> <li>- Adveres tissue reaction</li> </ul>	<ul style="list-style-type: none"> <li>- Elastic modulus</li> <li>- Tensile &amp; yield strength</li> <li>- Elongation</li> <li>- Toughness</li> <li>- Fatigue crack initiation, propagation</li> <li>- Hardness, wear resistance</li> </ul>

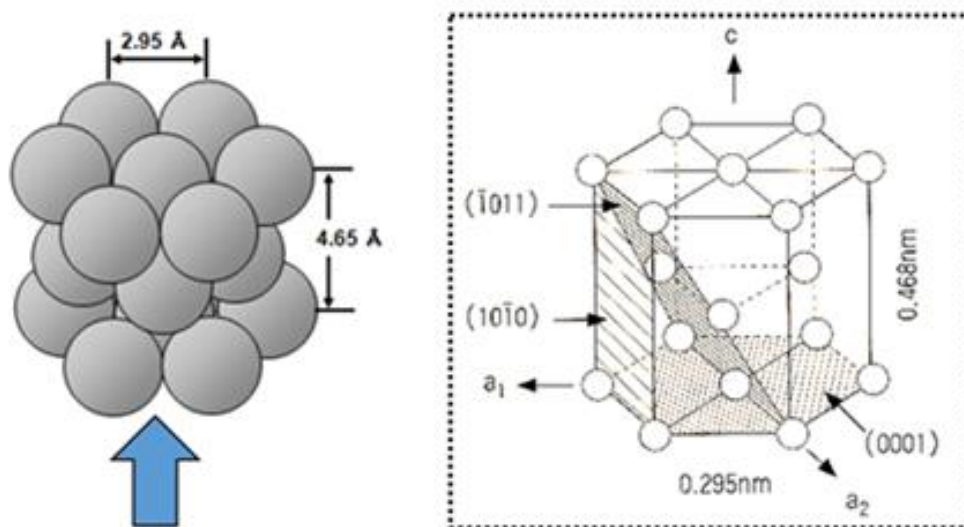
## 2.2. Titanium properties<sup>[21-25]</sup>

Since the Kroll process has caused commercial potential in ore in 1936, titanium, also referred to as the "marvelous metal," has been used in more and more specialized applications because the Kroll process has made this material a mine. Titanium is the most common element found on all continents and is recovered from  $TiO_2$ -rich deposits of rutile, ilmenite and leucoxene. Until titanium was discovered in 1794 and Kroll's innovative process development in 1936, there was no practical way to recover titanium metal from this ore because of its affinity for oxygen. Modern ore extraction, benzoylation and chemical processes have since made it possible to mass-produce titanium metal for the production of high-grade  $TiO_2$  and CP-Ti (commercial pure titanium) grades, important pigments in paints and commercial products, alloys and other alloy systems [21,22]. Metal biomaterials are classified as stainless steel, cobalt-based alloys, titanium metal and etc., and other materials include solid gold, dental amalgam, and other special metals. Titanium can be transformed into two crystallographic forms. CP-Ti has a hexagonal close-packed (hcp) crystal structure called  $\alpha$ -phase at room temperature. The crystallographic change of body-centered cubic (bcc) structure known as  $\beta$ -phase through the addition of alloying and thermochemical treatment at  $883^\circ\text{C}$  is shown in Fig 1. Titanium properties can lead to changes in alloying by bonding with other elements. The stabilization effects of the alloying elements are summarized in Table 3. The main requirements for all biocompatible materials, including metallics, are now understood with regard to corrosion resistance, biocompatibility, bioadhesive (bone ingrowth), mechanical properties, and availability [23-25].

### 2.2.1 Ti-Nb-Hf system[7-13,28-33]

Much research has been done on dental Ti alloying elements, focusing on alloys with Al and V added. So, focusing on Ti alloys, research on metallic biomaterials such as Ta, Hf, Nb and Zr composed of non-toxic elements are being conducted [7-9, 28-30]. Studies show that Ti-Nb alloys show great potential as implant materials. For example, Ti-25Nb has a bending strength of 1650 MPa and a bending strength of 77 GPa [10-13]. In addition, it is reported that Ti-Nb alloy shows excellent corrosion resistance when compared to Ti-6Al-4V alloy which is most used in dental field. Assis [31] also reported that the addition of Nb and Zr elements to Ti had slightly improved corrosion resistance compared to Ti-6Al-4V alloys. The Hf and Zr elements exhibit complete mutual solubility in both the  $\alpha$  and  $\beta$  structures with the Ti phase. Also Ti alloyed with Hf will likely to have good corrosion resistance [32-33]. In previously reported studies, the binding of Nb and Hf elements to Ti elements was spontaneously immobilized in 0.9% NaCl solution.  $I_{corr}$  and  $I_{pp}$  decreased slightly with increasing Hf content [12, 31-33].

HCP  
(Hexagonal close packed)



Crystal lattice  $\alpha$ -phase (below 882.5 °C)

B-phase (above 882.5 °C)

BCC  
(body centered cubic)

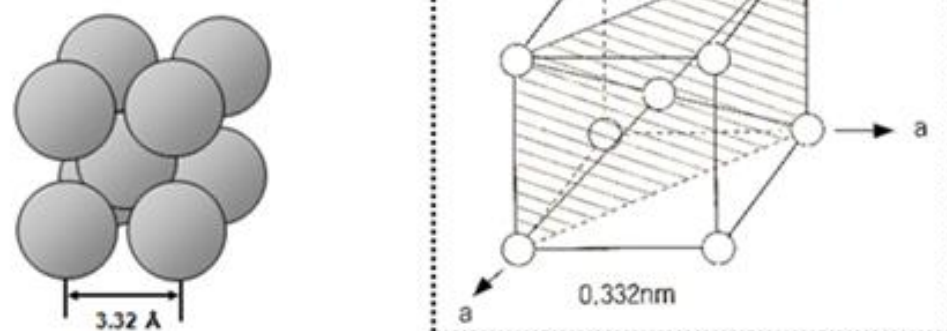


Fig. 1. Allotropic transformation of titanium [30].

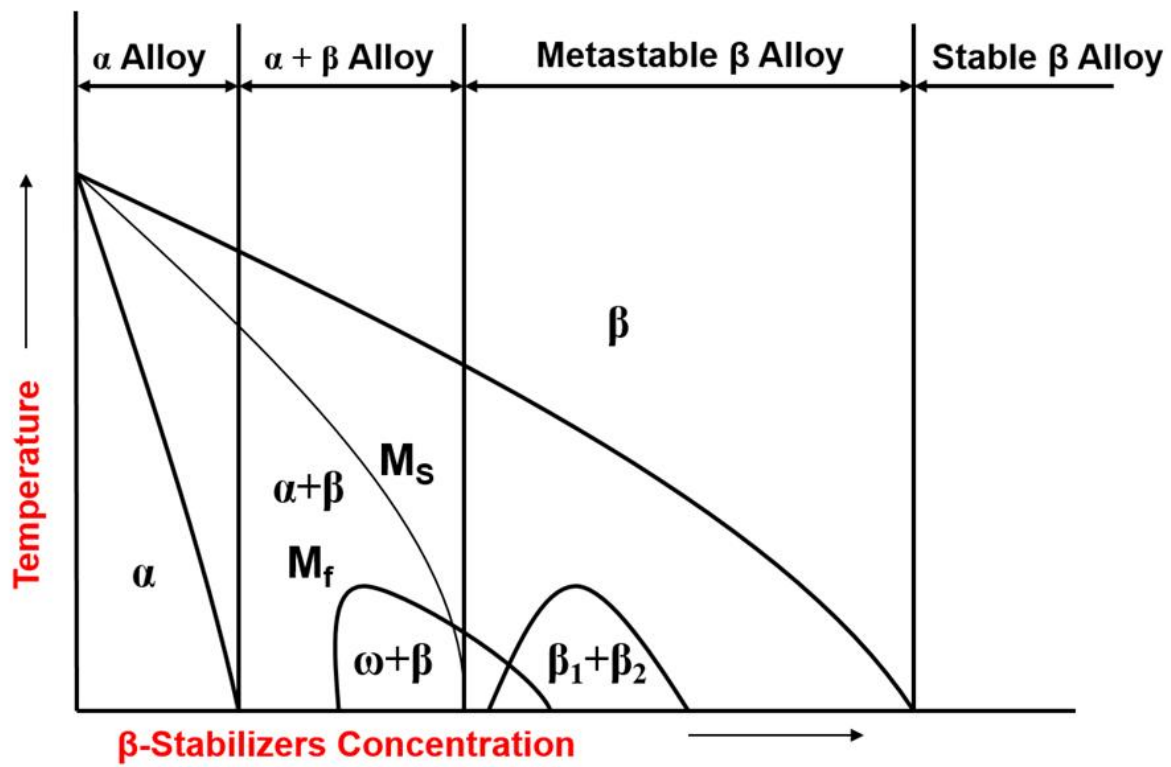


Fig. 2. Phase diagram of Ti and  $\beta$ -stabilization concentration [33].

Table 3. Physical property of titanium [9].

Property	Unit	Value
Density (20 °C)	g/cm <sup>3</sup>	4.54 (α-phase)
Melting point	°C	1688
Volume change in α-β transformation	%	5.5
α-β transformation temperature	°C	882.5
Thermal expansion coefficient (20 °C)	10 <sup>-6</sup> / °C	8.41
Thermal conductivity	cal/cm/cm <sup>2</sup> /°C/sec	0.035
Specific heat (20 °C)	cal/g	0.126
Electricity conductivity (about Cu)	%	2.2
Characteristics resistance (0 °C)	kΩ · cm	80
Elastic modulus	Gpa	103-107



## 2.3. Titanium oxide surface<sup>[35-38]</sup>

Titanium is known to form naturally on the surface of  $\text{TiO}_2$  oxide when exposed to air. It is known that the oxide film of thickness of several nanometers generated on the titanium surface has excellent chemical inertness, corrosion resistance, repassivation ability and biocompatibility due to its chemical stability and structure [35-38]. The composition of the mechanically polished CP-Ti surface and the oxide thickness indicated by X-ray photoelectron spectroscopy (XPS) are summarized in Table 4. The properties of the titanium oxide film grown at room temperature are shown in Table 5 and summarized as follows:

1.  $\text{TiO}_2$  oxide is mainly composed of amorphous or nanocrystalline oxide film with thickness of 3-7 nm.
2. The  $\text{TiO}_2$  /Ti interface has an O to Ti concentration ratio that varies gradually from 2 to 1 from the  $\text{TiO}_2$  to a much lower ratio in the bulk.
3.  $\text{TiO}_2$  induces biomolecules, and is surrounded by a glycoprotein layer that plays a role in recognizing cells or transporting chemicals between cells in vivo, and the implants quickly heal in the bone.

Table 4. Physical properties and crystal structure of  $\text{TiO}_2$ [35]

Property	Anatase	Rutile
Crystal structure	Tetragonal	Tetragonal
Atoms per unit cell (Z)	4	2
Space group	$I4_1/amd$	$P4_2/mnm$
Lattice parameters (Å)	$a = 3.7845$ $c = 4.5937$	$a = 0.4594$ $c = 2.9587$
Unit cell volume ( $\text{nm}^3$ )	0.1363	0.0624
Density ( $\text{g/cm}^3$ )	3.894	4.250
Calculated indirect band gap (eV)	3.23-3.59 (345.4-383.9 nm)	3.02-3.24 (382.7-410.1 nm)
Experimental band gap (eV)	$\sim 3.2$ ( $\sim 387$ nm)	$\sim 3.0$ ( $\sim 413$ nm)
Refractive index	2.54, 2.49	2.79, 2.903
Solubility in HF	Soluble	Insoluble
Solubility in $\text{H}_2\text{O}$	Insoluble	Insoluble
Hardness (Mohs)	5.5-6	6-6.5
Bulk modulus (GPa)	183	206

Crystal structure

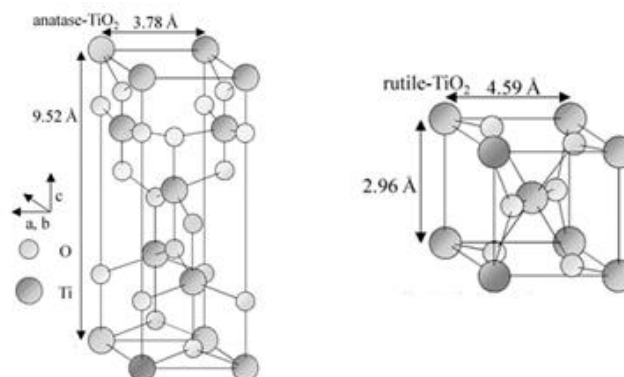


Table 5. Physicochemical properties of titanium oxide and other metal oxides [36-38]

Element	Most stable oxide	Isoelectric point	Charge at pH 7	Solubility at Ph 7 [mol/l]	Typical tissue response
<b>Ti</b>	TiO <sub>2</sub>	3.5-6.7	-	3*10 <sup>-6</sup>	Inertness
<b>Al</b>	Al <sub>2</sub> O <sub>3</sub>	8.8-9.5	+	10 <sup>-6</sup>	Sequestration
<b>Nb</b>	Nb <sub>2</sub> O <sub>5</sub>	3.4-3.8	-	~10 <sup>-5</sup>	Inertness
<b>V</b>	V <sub>2</sub> O <sub>5</sub> V <sub>2</sub> O <sub>4</sub>	11.5-2.3	-	> 1 ~10 <sup>-4</sup>	Toxicity
<b>Zr</b>	ZrO <sub>2</sub>	4,6,7,10-11		<10 <sup>-6</sup>	Inertness
<b>Ta</b>	Ta <sub>2</sub> O <sub>5</sub>	2.7-3	-	~10 <sup>-5</sup>	Inertness
<b>Fe</b>	Fe <sub>2</sub> O <sub>3</sub> FeO	2.2-9		<10 <sup>-10</sup> ~10 <sup>-11</sup>	Sequestration
<b>Cr</b>	Cr <sub>2</sub> O <sub>3</sub>	6.7-7.4	±0	~10 <sup>-11</sup>	Toxicity
<b>Co</b>	Co <sub>2</sub> O <sub>3</sub>	10.8	+	~10 <sup>-12</sup> (CoO)	Toxicity

## 2.4. Electrochemical anodization process[34].

Anodizing is an electrolytic process that creates an oxide film that increases the thickness and density of oxide films on metal surfaces. To achieve this, the conducting piece performing the anodizing treatment is located in the electrolyzer connected to the positive terminal of the power supply and acting as an anode. The cathode uses platinum plates or rods. The electrons are forced to move from the electrolyte to the anode when power is supplied. This process allows metal surface atoms to be exposed to oxygen ions in the electrolyte. The atoms react to form the in situ part of the oxide layer. When power is applied, the electrons return to the cathode, and the description of the electrochemical anodization cell is shown in Fig 3.

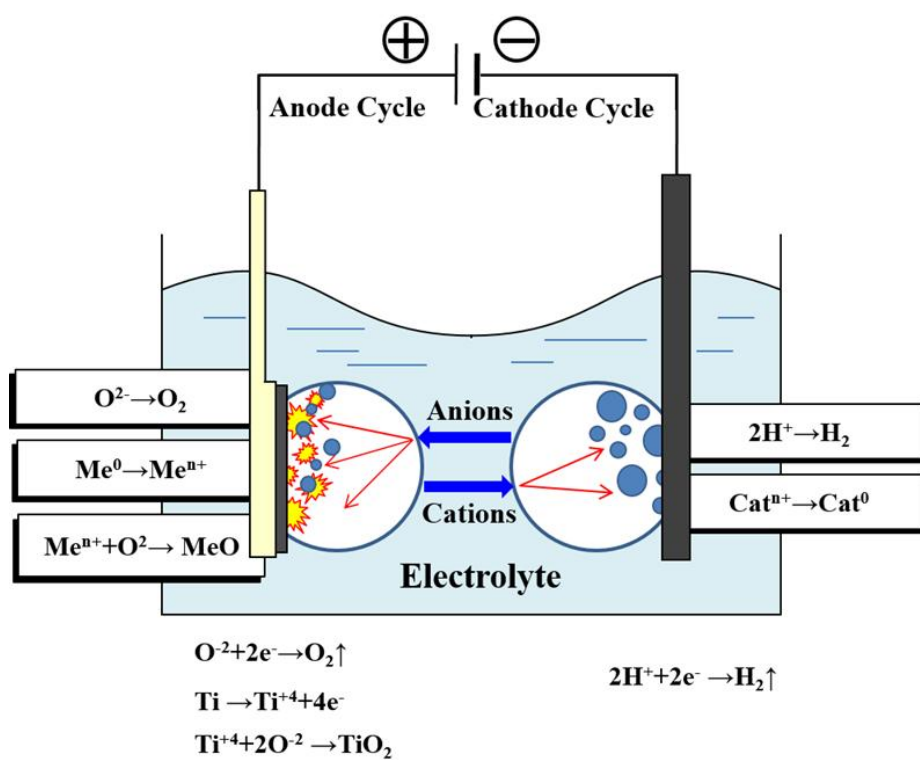


Fig. 3. Schematic diagram of electrode processes in electrolysis of aqueous solutions[34].

## 2.5. Micro-porous oxide formation[21-25, 35-38]

Ti and oxygen ions formed in this oxidation-reduction reaction are driven through oxides by an externally applied electric field to form an oxide film. The following reactions may occur:

- (1) Main reactions at the Ti / TiO<sub>2</sub> interface during the anodic oxidation are as follows:



- (2) At the TiO<sub>2</sub> /electrolyte interface:



- (3) At both interfaces:



The drop in the applied voltage occurs mainly across the oxide film of the anode, and the anode TiO<sub>2</sub> has a higher resistance than the metal portion of the electrolyte and the electric circuit. The oxide does not have sufficient resistance to prevent current flow when the anodizing treatment is higher than the breakdown voltage. The process at these high voltages is commonly referred to as spark anodizing and has a porous oxide film on its surface. Surgical insertion of Ti implants, such as cortical screw threads and some artificial tooth roots, involves significant wear. These applications prefer to have high adhesion and surface hardness on the implant surface. The anodic plasma oxidation of Ti has been developed to meet these requirements. When a positive voltage is applied to Ti, Ti atoms are ionized at the metal

oxide interface and oxygen is diffused through the oxide layer. They combine and the oxide becomes thicker. As oxide thickness increases, resistance also increases, and this layer accounts for most of the voltage drop. Surface deformations of Ti implants typically use voltages of several hundred volts. In this case, micro-arc causes local formation. The intense oxygen gas generated during the decomposition process has a temperature enough to melt the oxide, which has crater-shaped pores on the surface. Moreover, micrometer-scale porosity and topography can contribute to implant fixation by mechanical interlocking.

## 2.6. Effect of magnesium (Mg) and silicon (Si) in the bone<sup>[35-41]</sup>

Various mineral elements exist in the human body, and essential trace elements have been reported to play an important role in bone formation because they affect bone density. Information on the effect of the mineral element in the human body is shown in Table 6, and the content of the mineral element present in the human body is shown in Table 7. Among the various factors, magnesium (Mg) is one of the major substituents of calcium (Ca). The amounts contained in the enamel, dentin and bone were 0.2 wt%, 1.1 wt% and 0.6 wt%, respectively. Mg is the fourth most abundant ion in the human body, Mg is known as Ca substitute, and it has a structure that can be easily substituted in HA lattice. This substitution structure is represented by the formula  $\text{Ca}_{10-x}\text{Mg}_x(\text{PO}_4)_6(\text{OH})_2$ . Mg ions are known to play an important role in the proliferation of bone metabolism by inhibiting crystallization, stimulating nucleation of large amounts of apatite nuclei, and influencing osteoblast and osteoclast activity. In the bone, Mg stimulates irregular bones to convert them into more crystalline and mature bones. Substitution of magnesium in Ca-deficient HA lattice is expected to be comparable to hard tissue with excellent biocompatibility of Mg-HA. As a result of solubility, crystallinity and particle shape, the bioactivity is expected to be controlled by controlling the  $\text{Mg}^{2+}$  substitution in the Mg-HA solution window. Therefore, surface modification helps improve the activity between the implant and bone.

Silicone (Si) influences skeletal development and bone formation, which was established by Carlisle. In general, highly concentrated Si is present in metabolically active osteoblasts and is considered essential for extracellular matrix formation in bone and cartilage. In addition, a reduction in Si in bone results in a decrease in the number of osteoblasts, osseomatriceal collagen, and glycosaminoglycans. These findings suggest that



Si may affect the cellular response at the implant/bone interface, thereby influencing the rate of skeletal repair. Si has been shown to be involved in apatite formation and HA in osteoblastic activity and simulated body fluids (SBF).

Table 6. Effect of selected metallic ions on human bone metabolism and angiogenesis : summary of literature studies[35–38]

Ion	Biological response in vivo / in vitro
<b>Si</b>	<ul style="list-style-type: none"> <li>-essential for metabolic processes, formation and calcification of bone tissue</li> <li>-dietary intake of Si increases bone mineral density (BMD)</li> <li>-aqueous Si induces Hap precipitation</li> <li>-<math>\text{Si}(\text{OH})_4</math> stimulates collagen I formation and osteoblastic differentiation</li> </ul>
<b>Ca</b>	<ul style="list-style-type: none"> <li>-favours osteoblast proliferation, differentiation and extracellular matrix (ECM) mineralization</li> <li>-activates Ca-sensing receptors in osteoblast cells, increases expression of growth factors, e.g. IGF-I or IGF-II</li> </ul>
<b>P</b>	<ul style="list-style-type: none"> <li>-stimulates expression of matrix la protein (MGP) a key regulator in bone formation</li> </ul>
<b>Zn</b>	<ul style="list-style-type: none"> <li>-shows anti-inflammatory effect and stimulates bone formation in vitro by activation protein synthesis in osteoblasts</li> <li>-increases ATPase activity, regulates transcription of osteoblastic differentiation genes, e.g. collagen I, ALP, osteopontin and osteocalcin</li> </ul>
<b>Mg</b>	<ul style="list-style-type: none"> <li>-stimulates new bone formation</li> <li>-increases bone cell adhesion and stability (probably due to interactions with integrins)</li> </ul>
<b>Sr</b>	<ul style="list-style-type: none"> <li>-shows beneficial effects on bone cells and bone formation in vivo</li> <li>-promising agent for treating osteoporosis</li> </ul>
<b>Cu</b>	<ul style="list-style-type: none"> <li>-significant amounts of cellular Cu are found in human endothelial cells when undergoing angiogenesis</li> <li>-promotes synergetic stimulating effects on angiogenesis when associated with angiogenic growth factor FGF-2</li> <li>-stimulates proliferation of hman endothelial cells</li> <li>-induces differentiation of mesenchymal cells towards the osteogenic lineage</li> </ul>
<b>B</b>	<ul style="list-style-type: none"> <li>-stimulates RNA synthesis in fibroblast cells</li> <li>-dietary boron stimulates bone formation</li> </ul>

Table 7. Comparative composition of human enamel, dentin, and bone[37-41]

	<b>Enamel</b>	<b>Dentine</b>	<b>Bone</b>
<b>Ca (wt.%)</b>	37.6	40.3	36.6
<b>P (wt.%)</b>	18.3	18.6	17.1
<b>CO<sub>2</sub> (wt.%)</b>	3.0	4.8	4.8
<b>Na (wt.%)</b>	0.70	0.1	1.0
<b>K (wt.%)</b>	0.05	0.07	0.07
<b>Mg (wt.%)</b>	0.2	1.1	0.6
<b>Sr (wt.%)</b>	0.03	0.04	0.05
<b>Cl (wt.%)</b>	0.4	0.27	0.1
<b>F (wt.%)</b>	0.01	0.07	0.1
<b>Zn (ppm)</b>	263	173	39
<b>Ba (ppm)</b>	125	129	
<b>Fe (ppm)</b>	118	93	
<b>Al (ppm)</b>	86	69	
<b>Ag (ppm)</b>	0.6	2	
<b>Cr (ppm)</b>	1	2	0.33
<b>Co (ppm)</b>	0.1	1	<0.025
<b>Sb (ppm)</b>	1	0.7	
<b>Mn (ppm)</b>	0.6	0.6	0.17
<b>Au (ppm)</b>	0.1	0.07	
<b>Br (ppm)</b>	34	114	
<b>Si (ppm)</b>			500
<b>Ca/P</b>	1.59	1.67	1.65

### III . MATERIALS AND METHODS

#### 3.1. The preparation of Ti-29Nb-xHf alloys

The CP Ti (G&S Titanium, Grade 4, USA), Nb, and Hf (Kurt J. Lesker Company, 99.95 wt.% purity, USA) were used for making the Ti-29Nb-xHf ( $x = 0, 3, 7$  and  $15$ ) alloys. And prepared alloys were cleaned by ultrasonic cleaner with acetone and ethanol. After cleaning, all alloys were dried thoroughly.

The Ti-29Nb-xHf alloys were prepared by using the vacuum arc melting furnace (vacuum arc melting system, SVT, KOREA) at high-purity Ar gas. The gas was filled up to water cooling copper hearth in vacuum atmosphere. For keeping vacuum, atmosphere was controlled by chamber fine gage. To avoid inhomogeneity of Ti-29Nb-xHf alloys, ingots were remelted at least 10 times in Ar atmosphere at  $1050^{\circ}\text{C}$  (MSTF-1650, MS Eng, KOREA) for 12hrs, and then  $0^{\circ}\text{C}$  water quenching. The alloy ingots were cut off by using diamond wheel cutting system (Accutom-5, Struers, Denmark) by way of a thickness of 3.0 mm for experiments, and then ultrasonically cleaned in acetone and finally dried in air.

### 3.2. The characterization of Ti-29Nb-xHf alloys

The microstructure of the Ti-29Nb-xHf alloys were analyzed by optical microscopy (OM, Olympus BM60 M, Japan) after performing treatment in Keller's reagent (2 ml HF + 3 ml HCl + 5 ml  $\text{NH}_4\text{OH}$  + 190 ml  $\text{H}_2\text{O}$ ). The compositions of each alloys were identified by X-Ray fluorescence (XRF, Analyzer Serial number-581331, OLYMPUS, Japan), Analyzer Serial number-581331, OLYMPUS, Japan). The phase and composition of each alloy was observed by using X-ray diffractometer (XRD, X' pert PRO. Philips). The HCPDS files and characterization were used for matching each characteristic peak in this study.

### 3.3. Micro-pore formation on the alloy surface

The washed Ti-29Nb and Ti-29Nb-15Hf alloys were used as anodes and a carbon rod was used as the catode in different electrolytes containing Mg concentration of 0 Mol% (CaP), 5 Mol% (5Mg), 10 Mol% (10Mg), 20 Mol% (20Mg), as shown in Table 8. The concentration of the electrolytic solution was stirred during anodizing process in the beaker. The micro-pore formation was carried out using by DC power supply (KDP-1500, KOREA) at 270 V for 3 min as shown in Table 9. The current density was applied to 70 mA in anodizing process. The morphologies of micro-pore formed Ti-29Nb and Ti-29Nb-15Hf oxide were observed by a FE-SEM, EDS, and XRD. The image J (jhttp://rsb.info.nih.gov/i/, NIH, USA) software and image analyzer (Image Pro Plus, Media Cybernetics, PA, USA) were used for measuring the surface fraction of porosity and pore size from FE-SEM image of micro-pore formed alloy.

Table 8. The condition of different electrolytes containing plasma electrolytic oxidation.

Experimental Condition Specimen	Composition of Electrolyte			
	Calcium Acetate (mol L <sup>-1</sup> )	Calcium Glycerophosphate (mol L <sup>-1</sup> )	Magnesium acetate tetrahydrate (mol L <sup>-1</sup> )	Sodium Metasilicate (mol L <sup>-1</sup> )
CaP	0.15	0.02	0	0
5Mg/5Si	0.1425	0.02	0.0075	0.001
10Mg/5Si	0.135	0.02	0.015	0.001
20Mg/5Si	0.12	0.02	0.03	0.001

Table 9. The condition of plasma electrolytic oxidation.

<b>Working equipment</b>	KDP-1500, KOREA
<b>Working electrode</b>	Samples (Ti-29Nb and Ti-25Ta-15Hf alloy)
<b>Counter electrode</b>	High dense carbon
<b>Applied voltage</b>	270 V
<b>Applied current</b>	70 mA
<b>Time</b>	3 min



### 3.4. Measurement of mechanical properties

The elastic modulus ( $E$ ) and the hardness ( $H$ ) of the Ti-29Nb-xHf alloy were measured by using nano-indentation tester(TTX-NHT3, Anton paar, Austrial) and vickers hardness tester(DM-2D, AFFRI, Italy). The nano-indentation test was performed at allowable load range of 500 mN, a pulling speed of 25 N / min, depth range fine range 40  $\mu\text{m}$ , and large range 200  $\mu\text{m}$ . At least five indentation measures were obtained for each alloy in the nano-indentation test.

### 3.5. Surface wettability measurement

For performing wettability test, micro-pore surfaces of Ti-29Nb and Ti-29Nb-15Hf formed by PEO-treatment in electrolyte containing Ca, Mg, P, and Si ions, were used by water contact angle goniometer (Kruss DSA100, Germany). Surface wettability values were obtained through performing water contact angle test. The water contact angles were obtained by sessile droplet method and a video camera. At least ten water contact angle values were measured for each alloy with 6  $\mu\text{l}$  drop mode.

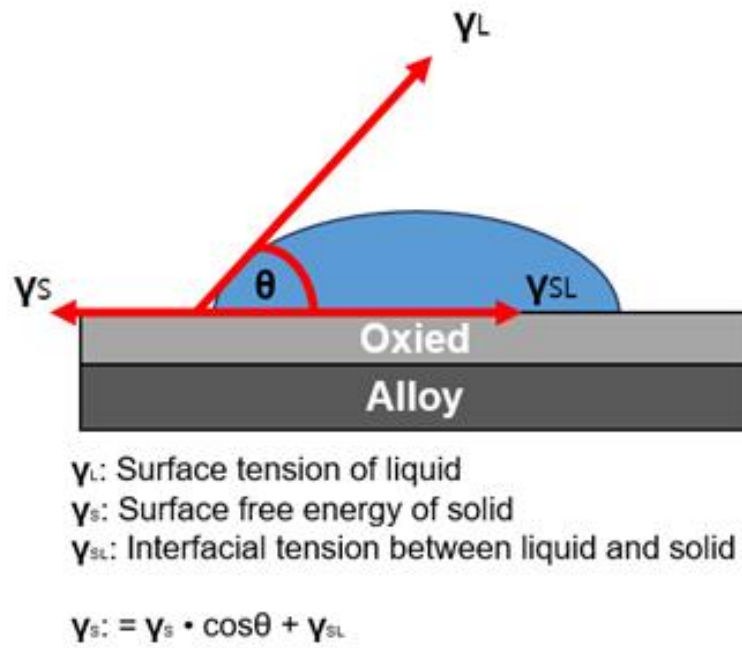


Fig. 4. Equilibrium wetting state of liquid.

### 3.6. Electrochemical tests

To evaluate the electrochemical characteristics of Ti-29Nb-xHf before and after PEO-treatment in a solution containing Mg. Potentiodynamic polarization and AC impedance tests were performed using a three-electrode electrochemical system. A specimen was connected to the working electrode, a saturated calomel electrode (SCE) was used as the reference electrode, and a high density carbon rod was used as the counter electrode. Argon gas was injected and stirred to remove impurities, oxides and dissolved oxygen. All specimens were allowed to stabilize in the electrolyte at the appropriate open circuit potential for 10 min before the start of the test. The specimens were used for each test, and mean values with the standard deviations of the corrosion parameters were obtained from the raw data. Potentiodynamic polarization and AC impedance tests were carried out using a potentiostat (Model 2273, EG&G Co. USA) using a 0.9% NaCl solution at  $36.5 \pm 1$  °C. The potential applied to the specimen was swept from the initial potential of -1500 to 2000 mV with scan rate of 100 mV/min, and the corrosion potential ( $E_{\text{corr}}$ ) and current density ( $I_{\text{corr}}$ ) were measured using a Tafel line analysis. An electrochemical impedance spectroscopy (EIS) test was performed at the open-circuit potential. A sinusoidal voltage of  $\pm 20$  mV was applied over a frequency range of 0.01 Hz to 100 kHz. Experimental results were interpreted assuming an equivalent circuit using the appropriate fitting procedure implemented in the ZSimpWin program (v.3.21, EChem Software, USA).

### 3.7. Formation of bone-like apatite in simulated body fluid

The PEO-treated Ti-29Nb and Ti-29Nb-15Hf specimens in solution containing Ca, P, Mg, and Si ions were prepared to examine the bioactivity in simulated body fluid (SBF) for 1 day. The ion concentrations of the SBF were listed in Table 10. Each specimen was placed in a beaker with SBF solution. The pH condition of SBF solution was kept in an incubator at 36.5 °C.

Table 10. Composition of SBF, in comparison with human blood plasma.

Ions	Concentration (mM)	
	Blood plasma	SBF
Na <sup>+</sup>	142.0	142.0
K <sup>+</sup>	5.0	5.0
Mg <sup>2+</sup>	1.5	1.5
Ca <sup>2+</sup>	2.5	2.5
Cl <sup>-</sup>	103.0	103.0
HCO <sub>3</sub> <sup>-</sup>	27.0	10.0
HPO <sub>4</sub> <sup>2-</sup>	1.0	1.0
SO <sub>4</sub> <sup>2-</sup>	0.5	0.5

### 3.8. MC3T3-E1 cell culture test

The mouse osteoblastic cell line MC3T3-E1(DSMZ, Braunschweig, Germany) was used in cell culture for 1day. Cells were grown in 12 well plates at a density of  $2 \times 10^5$  cells per 1 ml. And cells were routinely cultured on the he PEO-treated Ti-29Nb and Ti-29Nb-15Hf specimens in solution containing Ca, P, Mg, and Si ions in humidified atmosphere at 37°C for cell attachment observation. Cells cultured on each specimen were washed and fixed with phosphate buffered saline (PBS) and 4% buffered neutral formalin for cell adhesion. After fixing, the morphology analysis of the attached cells were observed using by field-emission scanning electron microscopy (FE-SEM).

## IV. RESULTS AND DISCUSSION

### 4.1. Microstructure observation of Ti-29Nb-xHf alloys

Fig. 5 shows optical microscopy (OM) images of Ti-29Nb-xHf alloys by different Hf contents (0, 3, 7, and 15 wt. %) after chemical etching in Keller's solution. Fig. 5 (a) is Ti-29Nb, (b) is Ti-29Nb-3Hf, (c) is Ti-29Nb-7Hf, and (d) is Ti-29Nb-15Hf alloy, respectively. The microstructure of the Ti-29Nb alloy showed needle-like structure in grain. And needle-like structure changed to an equiaxed grain structure with increasing Hf content. These needle-like structures were disappeared in Fig. 5(d). This phenomena suggest that the structure change with increasing Hf content in the Ti-29Nb-xHf alloys has the same role of increasing compositional Zr content in other alloys. It has  $\beta$ -stabilizing Hf and Nb with chemically similar properties [10,18].

Fig. 6 shows the X-ray fluorescence (XRF) analysis results of Ti-29Nb-xHf alloy after heat treatment at 1050 °C for 12hrs in Ar atmosphere, followed by 0 °C water quenching. Fig. 6 (a) is Ti-29Nb, (b) is Ti-29Nb-3Hf, (c) is Ti-29Nb-7Hf, and (d) is Ti-29Nb-15Hf alloy, respectively. The XRF results indicated that the elements of Ti-29Nb-xHf alloys were detected for Ti, Nb, and Hf. As a result, it was confirmed that the prepared alloys were in good agreement with the designed alloy.

Fig. 7 shows the XRD analysis results of Ti-29Nb-xHf alloy. Fig. 7 (a) is Ti-29Nb, (b) is Ti-29Nb-3Hf, (c) is Ti-29Nb-7Hf, and (d) is Ti-29Nb-15Hf alloy, respectively. The peaks of  $\alpha''$  phase showed higher intensity such as (100), (020), (101), and (021) in Fig. 7 (a) Ti-29Nb alloy compared to alloys. Especially, Fig. 7 (b) Ti-29Nb-3Hf and Fig. 7 (c) Ti-29Nb-7Hf alloys showed the  $\alpha'' + \beta$  phases. However, in the case of Fig. 7 (d) Ti-29Nb-15Hf alloys, the  $\beta$  phase peaks such as (110), (200), and (211) have higher



intensity compared to other alloys, change with increasing Hf content. From the previous study, Hf content of above 15 wt.% in Ti-Nb binary alloys was changed needle-like to equiaxed microstructure and  $\alpha''$  to  $\beta$ -phase [19]. It is confirmed that needle-like microstructure is mainly composed of  $\alpha''$ -phase and equiaxed microstructure mainly consists of  $\beta$ -phase as shown in Fig. 5.

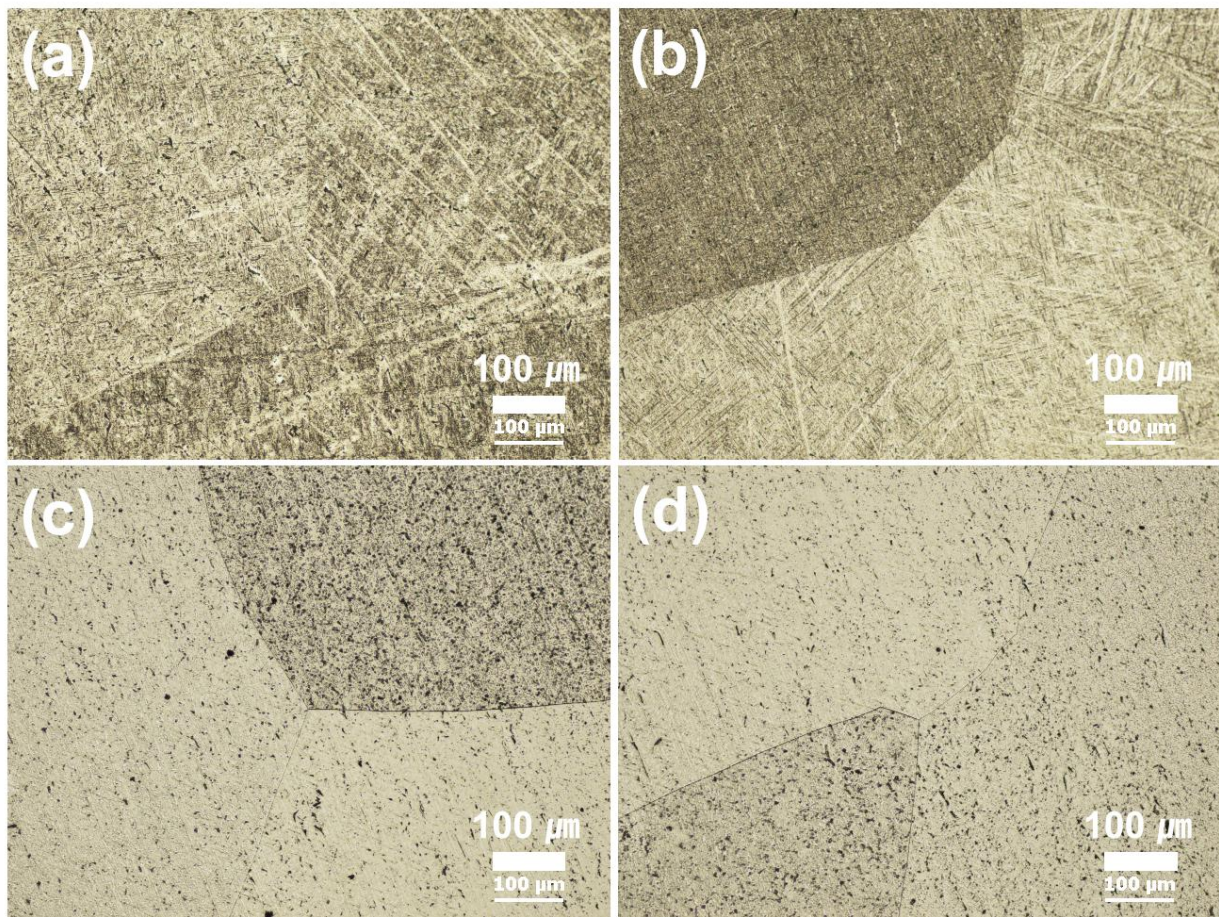


Fig. 5. OM images of Ti-29Nb-xHf alloys after heat treatment at 1050 °C for 12hrs in Ar atmosphere, followed by 0 °C water quenching: (a) Ti-29Nb, (b) Ti-25Nb-3Hf, (c) Ti-29Nb-7Hf, and (d) Ti-29Nb-15Hf.

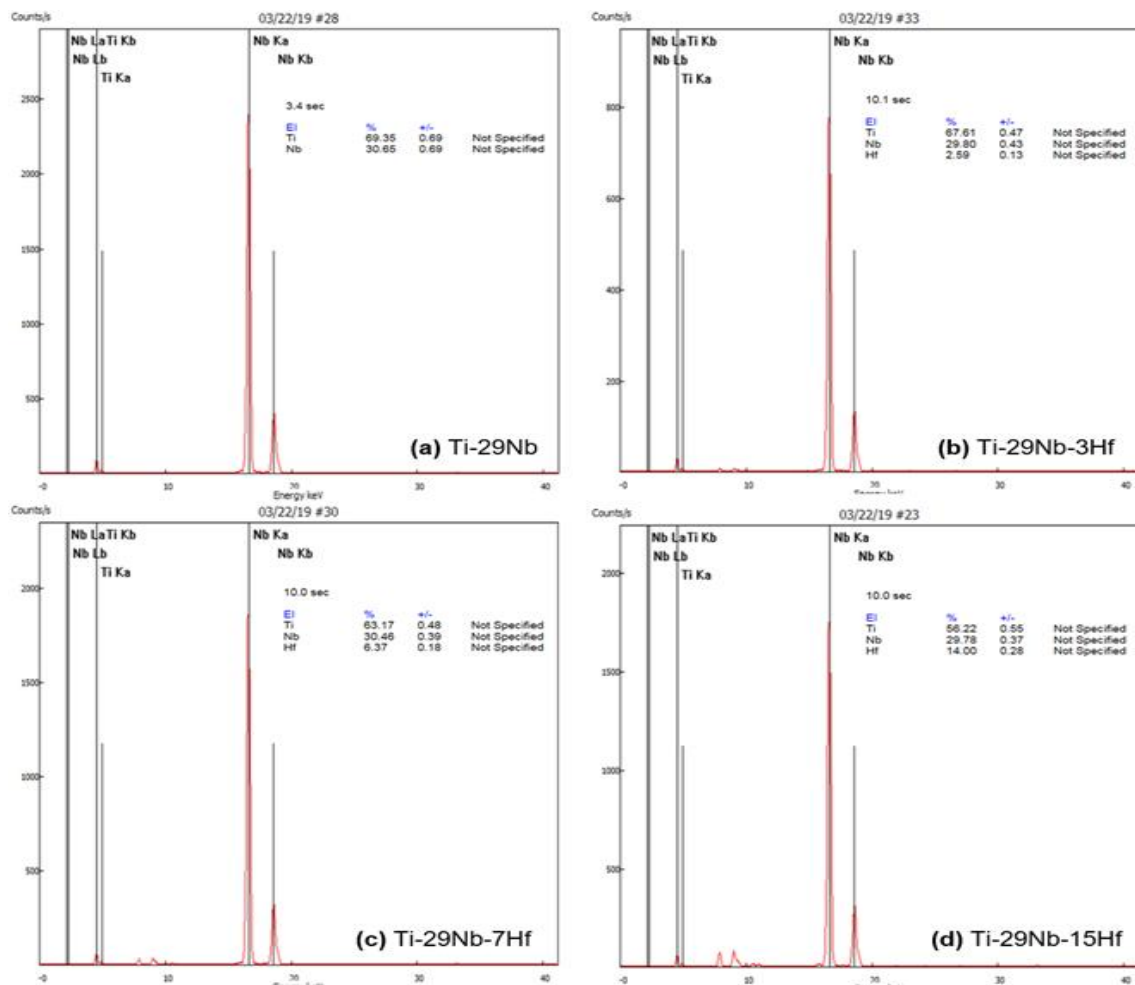


Fig. 6. XRF analysis results of Ti-29Nb-xHf alloys after heat treatment at 1050 °C for 12hrs in Ar atmosphere, followed by 0 °C water quenching: (a) Ti-29Nb, (b) Ti-29Nb-3Hf, (c) Ti-29Nb-7Hf, and (d) Ti-29Nb-15Hf.

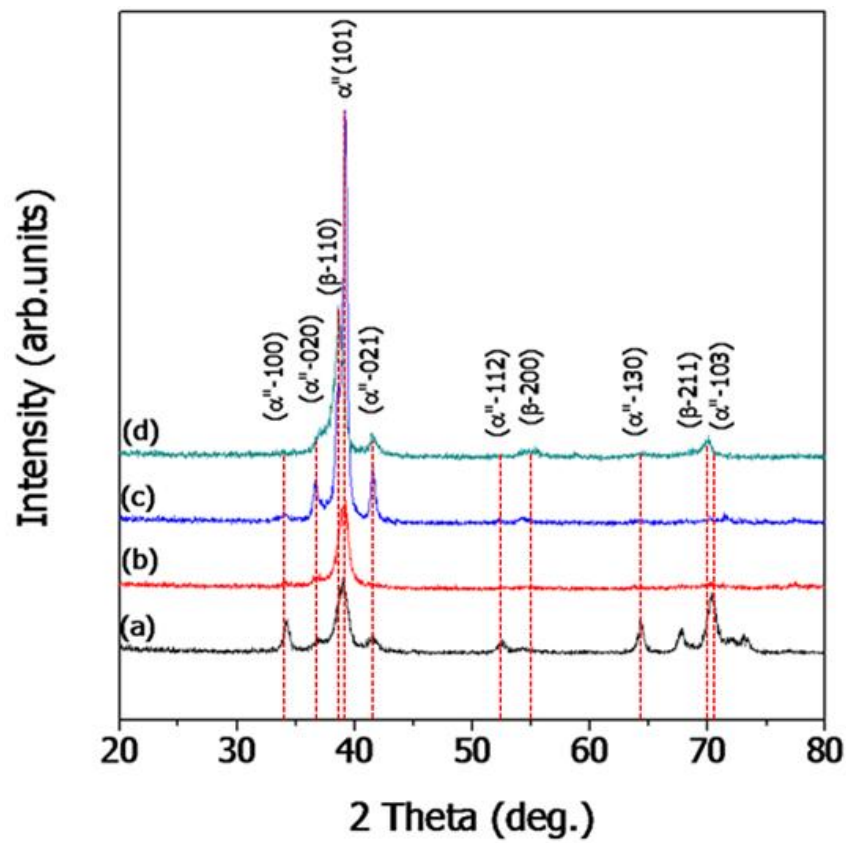


Fig. 7. XRD analysis results of Ti-29Nb-xHf alloys after heat treatment at 1050 °C for 12hrs in Ar atmosphere, followed by 0 °C water quenching: (a) Ti-29Nb, (b) Ti-29Nb-3Hf, (c) Ti-29Nb-7Hf, and (d) Ti-29Nb-15Hf [42].

## 4.2. Corrosion behavior of Ti-29Nb-xHf alloys

Fig. 8 shows the potentiodynamic polarization curves of Ti-29Nb-xHf alloys ( $x = 0, 3, 7$ , and  $15$ ) for various samples in a  $0.9\%$  NaCl solution at  $36.5 \pm 1$  °C. As a result, the corrosion potential ( $E_{\text{corr}}$ ) values of Ti-29Nb-3Hf, Ti-29Nb-7Hf, and Ti-29Nb-15Hf alloys are  $-470$  mV,  $-450$  mV, and  $-370$  mV. It is exhibited that increasing Hf element serves nobler  $E_{\text{corr}}$  values than the Ti-29Nb ( $-602$  mV) without Hf element. And corrosion current density ( $i_{\text{corr}}$ ) value of Ti-29Nb is  $6.90 \times 10^{-7} \text{ A} \cdot \text{cm}^{-2}$ , Ti-29Nb-3Hf is  $8.78 \times 10^{-7} \text{ A} \cdot \text{cm}^{-2}$ , Ti-29Nb-7Hf is  $8.84 \times 10^{-7} \text{ A} \cdot \text{cm}^{-2}$ , and Ti-29Nb-15Hf is  $7.02 \times 10^{-7} \text{ A} \cdot \text{cm}^{-2}$ . The  $i_{\text{corr}}$  value of Ti-29Nb-15Hf decreased slightly from  $8.78 \times 10^{-7} \text{ A} \cdot \text{cm}^{-2}$  to  $7.02 \times 10^{-7} \text{ A} \cdot \text{cm}^{-2}$ . Furthermore, in the potentiodynamic plots, the Ti-29Nb-15Hf alloy exhibited the highest corrosion resistance. These results suggested that, upon addition of Hf, the passive area was significantly enlarged. Generally, Hf as an alloying element plays a crucial role in inhibiting the aggressive chloride ions present in solution. The corrosion current density was evaluated by using the based on a software approximation. The corrosion potential ( $E_{\text{corr}}$ ), current density at  $300$  mV ( $i_{300\text{mV}}$ ), corrosion current density ( $i_{\text{corr}}$ ), and primary passivation potential ( $E_{\text{pp}}$ ) from the summary of potentiodynamic polarization curve are reported in Table 11. Therefore, the corrosion potential found in alloys containing Hf is higher than that observed in alloys without Hf [8-13, 42].

Fig. 9 shows the Bode-plots and Bode-phase for Ti-29Nb, Ti-29Nb-3Hf, Ti-29Nb-7Hf, and Ti-29Nb-15Hf alloys after AC impedance test in  $0.9\%$  NaCl solution at  $36.5 \pm 1$  °C. Fig. 9 (a) is Bode-plots and (b) is Bode-phase plots. The electrochemical values of Ti-29Nb-xHf alloys were obtained from Bode-plots and Bode-phase plots by ZsimpWin software to simulate the equivalent circuit of bulk Ti alloy with anodic oxide layer in  $0.9\%$  NaCl solution system. Suitable values were found to fit the model presented in Fig. 10, and the approximated line in Fig. 9 generated by this model proved



appropriate data. It can be seen that the result of the systematic error was fitted as shown in Table 11, suggesting that this model provided a reliable description of the electrochemical system. As shown in Fig. 9, the experimental AC impedance data results for untreated Ti-29Nb-xHf alloys were obtained through the solution resistance ( $R_s$ ), polarization resistance ( $R_p$ ), constant phase elements (CPE), and empirical exponent of the CPE ( $n$ ) calculation values. From Fig. 9 the untreated Ti-29Nb, Ti-29Nb-3Hf, Ti-29Nb-7Hf and Ti-29Nb-15Hf alloy showed a stable passivating film on a phase angle near  $90^\circ$  in the mid-low frequency range. It is thought that the increase in impedance from Bode plot can be considered that the intermediate frequency region is related to the naturally formed stable oxide film in 0.9% NaCl solution [43-45].

Fig. 11 shows the OM images of Ti-29Nb-xHf alloys after potentiodynamic test in 0.9% NaCl solution at  $36.5 \pm 1^\circ\text{C}$ . Fig. 11 (a) is Ti-29Nb, (b) is Ti-29Nb-3Hf, (c) is Ti-29Nb-7Hf, and (d) is Ti-29Nb-15Hf. The microstructure of the (a) Ti-29Nb alloy showed the corroded area with black spots on the surface. The corroded area on the Ti-29Nb-15Hf was decreased compared to others. It is thought that addition of Hf to Ti-29Nb-xHf alloys can be increased the corrosion resistance due to stable passive film on the surface.

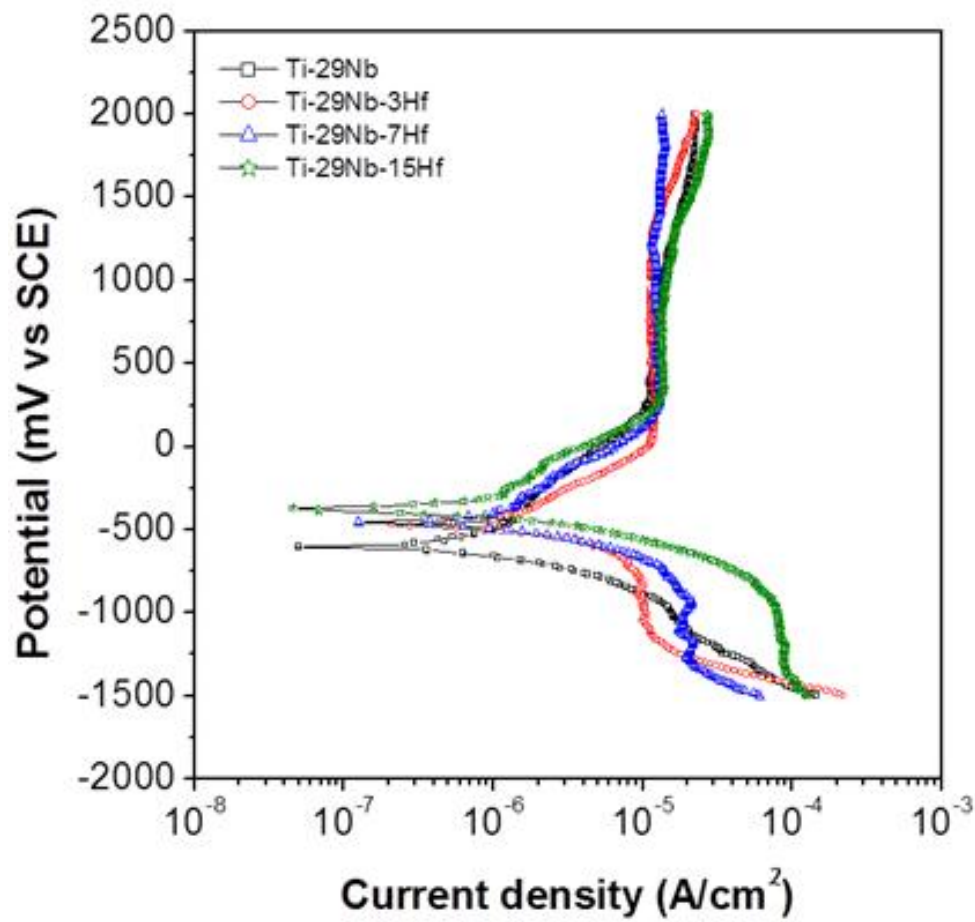


Fig. 8. Anodic polarization curves of Ti-29Nb-xHf alloys after potentiodynamic test in 0.9% NaCl solution at  $36.5 \pm 1^\circ \text{C}$ .

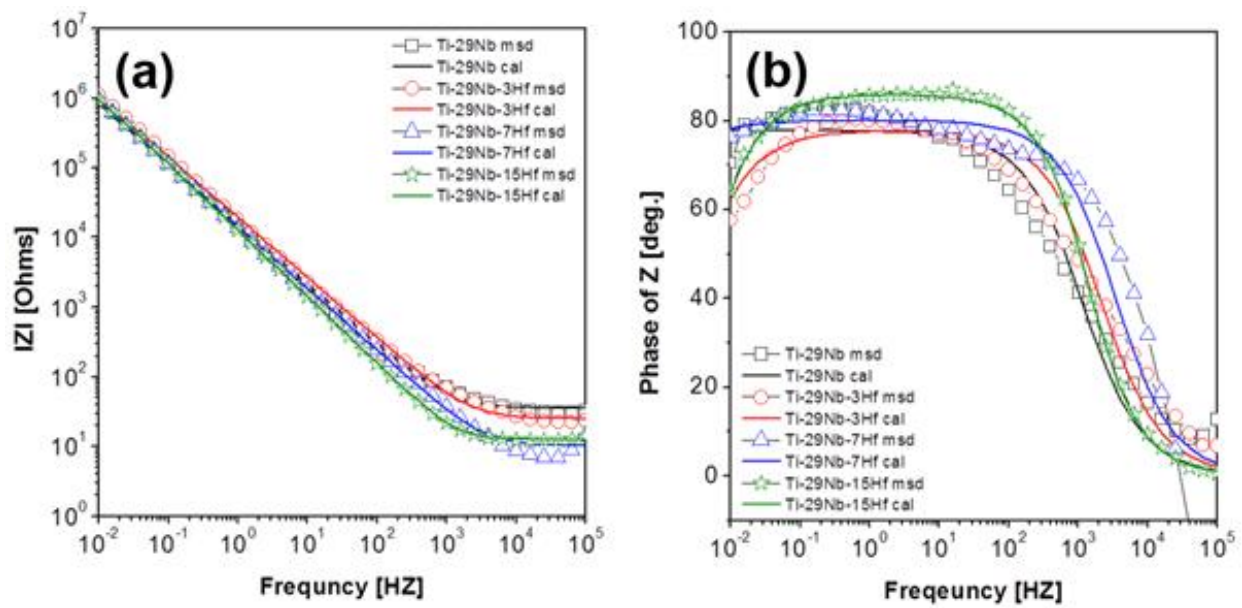


Fig. 9. Bode-plots and Bode-phase for Ti-29Nb-xHf alloys after AC impedance test in 0.9% NaCl solution at  $36.5 \pm 1^\circ \text{C}$  : (a) Bode-plots and (b) Bode-phase plots.





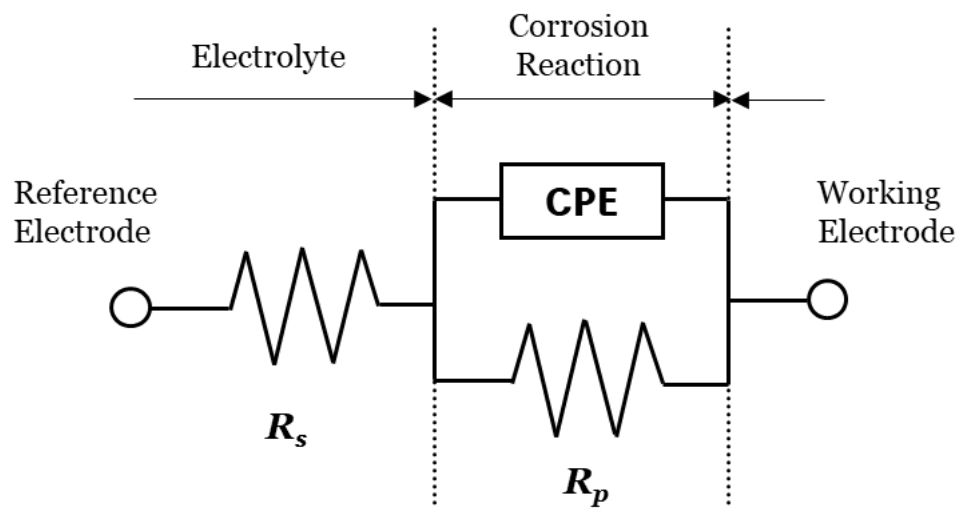


Fig. 10. Equivalent circuit of bulk Ti-29Nb-xHf alloys with anodic oxide layer [44].

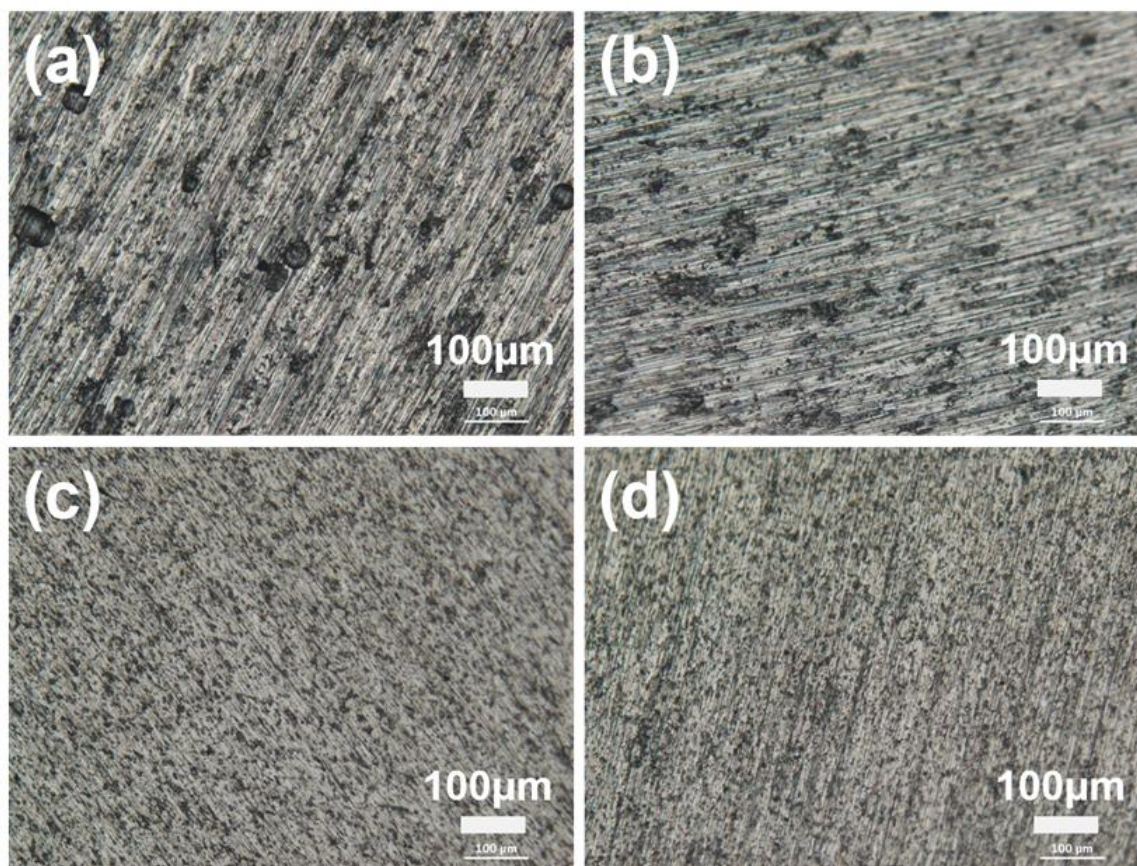


Fig. 11. Corrosion morphologies of Ti-29Nb-xHf alloys after potentiodynamic test in 0.9% NaCl solution at  $36.5 \pm 1$  °C: (a) Ti-29Nb, (b) Ti-25Nb-3Hf, (c) Ti-29Nb-7Hf, and (d) Ti-29Nb-15Hf.

### 4.3. Mechanical properties of Ti-29Nb-xHf alloys

Fig. 12 shows the Vickers hardness results of Ti-29Nb-xHf alloys. Fig. 12 is (a) Ti-29Nb, (b) is Ti-29Nb-3Hf, (c) is Ti-29Nb-7Hf, and (d) is Ti-29Nb-15Hf. The Vickers hardness results of water quenched Ti-29Nb-xHf alloys are shown in Table 12. The value of Vickers hardness for Ti-29Nb alloy was  $200.4 \pm 5.66\text{Hv}$ , while the corresponding values for the Ti-29Nb-3Hf, Ti-29Nb-7Hf, and Ti-29Nb-15Hf alloys were  $189 \pm 7.96\text{Hv}$ ,  $186 \pm 3.19\text{Hv}$ , and  $185 \pm 4.24\text{Hv}$ , respectively. Furthermore, the value of Vickers hardness decreased slightly as the Hf element increase. The content of Hf increases, phase transformation from  $\alpha''$ -hexagonal structure to the  $\beta$ -body-centered cubic was occurred and the alloy becomes sensitive to the indentation, resulting in a lower hardness value [46-50]. In the case of addition of Hf content to Ti-29Nb alloy, needle-like structure of  $\alpha''$  phase changed to an equiaxed grain structure of  $\beta$  phase, therefore, the value of Vickers hardness was lowered. It is assumed that the control of the metastable  $\alpha''$  martensitic phase and stability of  $\beta$  phase were related to addition of Hf element during the water quenching process [46-52].

Fig. 13 shows the nano-indentation test results of elastic modulus measurements of Ti-29Nb-xHf alloys. The elastic modulus was measured using by nano-indentation. The nano-indentation test results of water quenched Ti-29Nb-xHf alloys are shown in Table 12. The results of elastic modulus for Ti-29Nb alloy was  $99.29 \pm 2.00\text{ GPa}$ , while the corresponding results for the Ti-29Nb-3Hf, Ti-29Nb-7Hf, and Ti-29Nb-15Hf alloys were  $94.71 \pm 2.36$ ,  $94.36 \pm 2.31$ , and  $88.04 \pm 1.92$ , respectively. The low elastic modulus was the Ti-29Nb-15Hf alloy with the highest content of Hf compared with other alloys. It is shown that the elastic modulus decrease gradually with addition Hf increased. It is reported that the value reduction of elastic modulus was related to the  $\beta$  phase increases [42]. It is reported that the value of elastic modulus decreases with the  $\beta$  phase increases. Control of

the elastic modulus to lower the stress shielding effect can prevent bone resorption and bone destruction [42-44]. Therefore, value reduction of elastic modulus can be obtained from the addition of Hf element into the Ti-29Nb alloy.

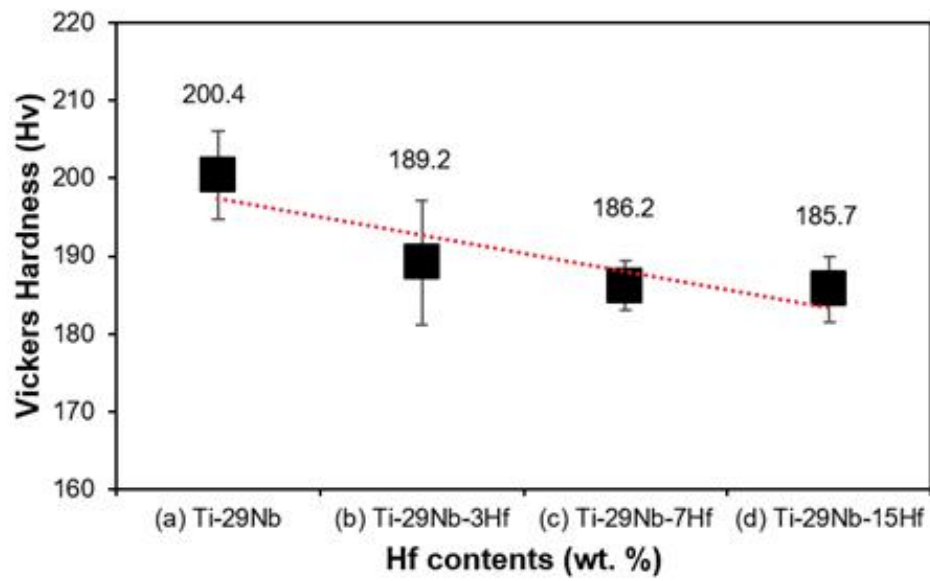


Fig. 12. Vicker' s hardness graph of Ti-29Nb-xHf alloys: (a) Ti-29Nb, (b) Ti-29Nb-3Hf, (c) Ti-29Nb-7Hf, and (d) Ti-29Nb-15Hf

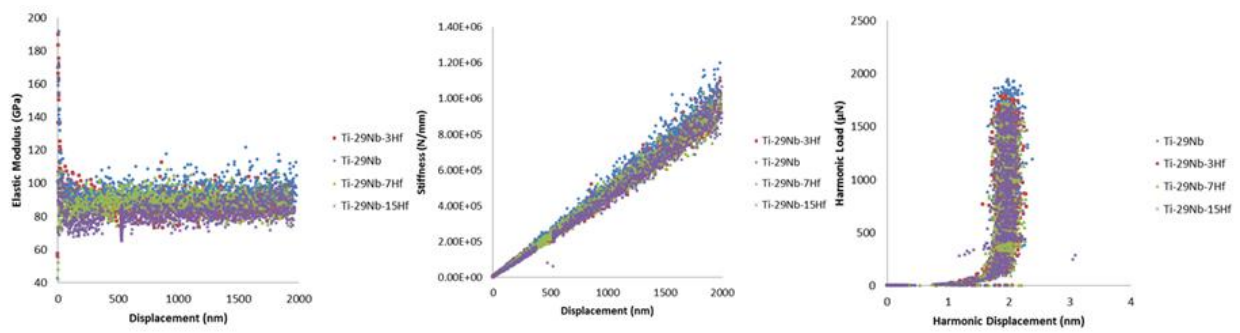


Fig. 13. Nano-indentation test results of Ti-29Nb-xHf alloys.

Table 12. Vicker' s hardness values of Ti-29Nb-xHf alloy.

Samples / Properties	Young's Modulus (E)	Vickers Hardness
	[GPa]	[Hv]
<b>Ti-29Nb</b>	99.29 ± 2.00	200.4 ± 5.66
<b>Ti-29Nb-3Hf</b>	94.71 ± 2.36	189.2 ± 7.96
<b>Ti-29Nb-7Hf</b>	94.36 ± 2.31	186.2 ± 3.19
<b>Ti-29Nb-15Hf</b>	88.04 ± 1.92	185.7 ± 4.24



#### 4.4. Micro-pore formation on the alloy surface

Fig. 14 shows the FE-SEM morphologies of PEO treated Ti-29Nb alloy. Fig. 14 (a) is low-magnification ( $\times 5,000$ ), and (b) is high-magnification ( $\times 50,000$ ). Anodization treatment was performed at 270 V for 3 min on the Ti-29Nb alloy. After PEO coating result, surface showed formation of micro-pores with uniform distribution on the surface of alloys. Fig. 14 shows the small holes on oxide film are formed in the large holes. This is thought to trigger the increase in gas evolution on the Ti alloy surface. This formation of micro-porous is caused by sparks when processing PEO. In a short time, rough surfaces and various porous oxide films can be obtained [53–55]. The various porous oxide films of Ti alloy can be controlled by anodizing time in anodizing process.

Fig. 15 shows the FE-SEM morphologies of PEO treated Ti-29Nb alloy(a, b, c, and d) and Ti-29Nb-xHf alloy(a-1, b-1, c-1, and d-1) with different electrolytes containing Mg concentration of (a and a-1) 0 Mg (b and b-1) 5 Mg, (c and c-1) 10 Mg, and (d and d-1) 20 Mg, respectively. Anodization treatment was performed at 270 V for 3 min on Ti-29Nb and Ti-29Nb-15Hf alloys with ions (Ca, P, Mg, Si). The various types of micro-porous oxide layers were formed as shown in Fig. 15. The number of micro-pore increased with increasing Mg concentration, whereas, the size of micro-pore decreased with increasing Mg concentration. Also, the number and the size of micro-pore formed Ti-29Nb-15Hf alloy were occurred with the tendency like Ti-29Nb alloy with increasing Mg concentration. And chemical composition of oxide layer was investigated by EDS analysis. It was confirmed that the oxide films on Ti-29Nb and Ti-29Nb-15Hf alloy were in good on the composed of the alloying elements, including ions (Ca, P, Mg, Si) and oxygen. In the PEO process, anodic compounds with Mg and Si ions in electrolyte drawn into discharge channel due to electric fields, and competition of Mg and Si ions in the solution are occurred for substitution with Ca and P. In the case of

$Mg^{2+}$  ions, the dehydration of aqueous ions, which needs to occur before incorporation into the crystalline structure, is slow. Also, it thought that the smaller ionic radius of  $Mg^{2+}$  (0.0069nm) might also affect the substitution for  $Ca^{2+}$  (0.099nm) in apatite [53–60].

Fig. 16 shows the FE-SEM and images of micro-pore distribution formed Ti-29Nb and Ti-29Nb-15Hf alloy by PEO processing with different electrolytes containing Mg concentration of (a and a-1) 0 Mg (b and b-1) 5 Mg, (c and c-1) 10 Mg, and (d and d-1) 20 Mg. The summarized values for the micro-pore formed on Ti-29Nb and Ti-29Nb-15Hf alloy were obtained using by Image J software (<http://rsb.info.nih.gov/ij/>, NIH, USA) and Image analyzer software (Image Pro Plus, Media Cybernetics, PA, USA). Fig. 16(a) is 0Mg, Fig. 16(b) is 5Mg, Fig. 16(c) is 10Mg, and Fig. 16(d) is 20Mg for Ti-29Nb alloy. And Fig. 16(a-1) is 0Mg, Fig. 16(b) is 5Mg, Fig. 16(c) is 10Mg, and Fig. 16(d) is 20Mg for Ti-29Nb-15Hf alloy, respectively. It shows the change of the number of pores and the size of pores according to the Mg concentration in the electrolyte. The average numbers of micro-pore formed on Ti-29Nb alloy by changing the Mg concentration at 270 V for 3 min were  $22.98 \pm 1.77$  for 0Mg,  $31.35 \pm 1.75$  for 5Mg,  $54.33 \pm 1.34$  for 10Mg, and  $59.45 \pm 0.15$  for 20Mg, respectively. The average numbers of micro-pore fabricated by changing the Mg concentration from Ti-29Nb-15Hf alloy at 270 V for 3 min were  $23.43 \pm 2.11$  for 0Mg,  $31.66 \pm 2.32$  for 5Mg,  $55.67 \pm 1.54$  for 10Mg, and  $60.77 \pm 0.23$  for 20Mg, respectively. It is confirmed that the numbers of micro-pore depends on the composition of electrolyte with added ions and the chemical composition of the alloy. In the case of the Ti-29Nb alloy, as the Mg concentration increased from 0Mg to 20Mg for a constant alloy composition, the mean pore size decreased drastically from  $1.35 \pm 0.09$  to  $0.83 \pm 0.29$ . It is thought that the activation energy depend on the increasing Mg concentration in the solution to attack on the alloy surface leading to the a small size of micro-pore formation gradually. In the case of the Ti-29Nb-15Hf alloy, as the Mg concentration increased from 0Mg to 20Mg for a constant alloy composition, the mean pore size decreased drastically from

$1.51 \pm 0.08$  to  $0.89 \pm 0.34$ . The area ratio of occupied micro-pore for Ti-29Nb alloy with increasing Mg concentration was  $10.59 \pm 0.33$ ,  $11.02 \pm 0.47$ ,  $12.17 \pm 0.55$ , and  $13.15 \pm 0.32$  and the area ratio of occupied micro-pore for Ti-29Nb-15Hf alloy with increasing Mg concentration was  $9.83 \pm 0.29$ ,  $10.99 \pm 0.44$ ,  $12.38 \pm 0.51$ , and  $13.11 \pm 0.41$ , respectively. The values of the micro-pore number and layer sizes for the Ti-29Nb and Ti-29Nb-15Hf alloy with different Mg concentration are shown in Table 13.

Fig. 17 shows the EDS mapping analysis results of PEO-treated (a) Ti-29Nb and (b) Ti-29Nb-15Hf alloys in Ca, P, Mg, and Si electrolyte, respectively. As a result of the EDS mapping analysis, Ca/P ratio was obtained by oxide film and was found the distribution degree of doping of ions. In Fig. 17, Ca / P ratios were determined on the oxide film surface, it is summarized in Table 14 and Fig. 18. Ti-29Nb and Ti-29Nb-15Hf alloy were observed 1.62 and 1.64 for Ca / P ratio. Also, as the content of added Mg increased, the ratio of Ca / P tended to decrease. In same concentration of electrolyte, the Ca / P ratio decreased with increasing Mg content. It is considered that there is a transition zone consisting of Ca, P, Mg, Si and O complexes between the exterior and interior of the coating material. Therefore, it is thought that Mg and Si ions on the PEO-treated implant surfaces serve a biocompatibility and good effect on cell and bone binding [45-47, 60-63].

Fig. 19 shows the TF-XRD patterns of PEO treated Ti-29Nb and Ti-29Nb-15Hf alloy with different electrolytes containing Mg concentration of (a) 0 Mg, (b) 5 Mg, (c) 10 Mg, and (d) 20 Mg, respectively. The peaks of  $\text{TiO}_2$  consisted predominantly of anatase with small amount of rutile, which was mixture structure as shown in the surface of the micro-pore formed Ti-29Nb and Ti-29Nb-15Hf alloys. Regarding with this result, the hydroxyapatite and anatase phases are believed to have more efficient nucleation and growth than the rutile layer because of their good lattice match [64-66].

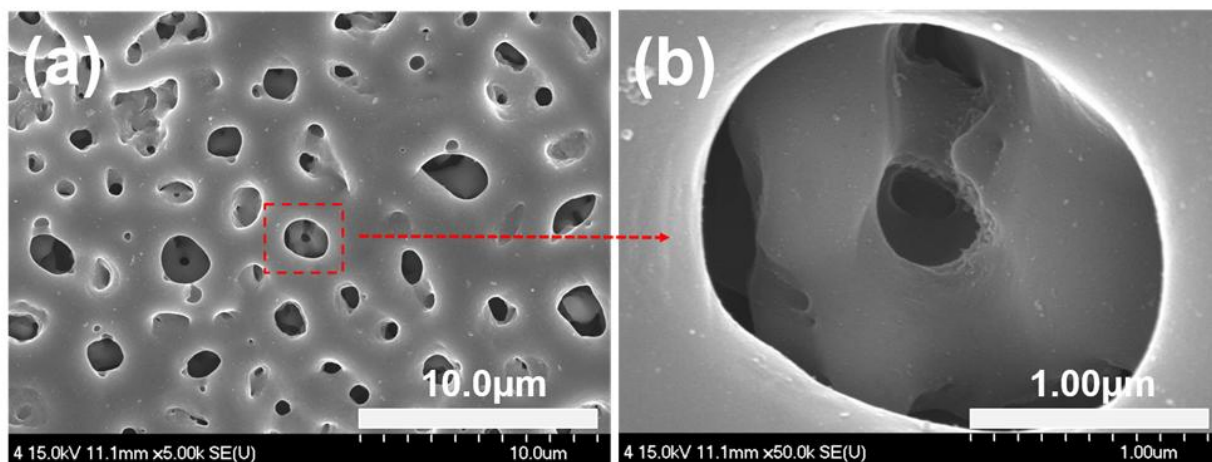


Fig. 14. FE-SEM images showing morphologies of PEO-treated Ti-29Nb alloy: (a) low-magnification (x 5,000) and (b) high-magnification (x 50,000).

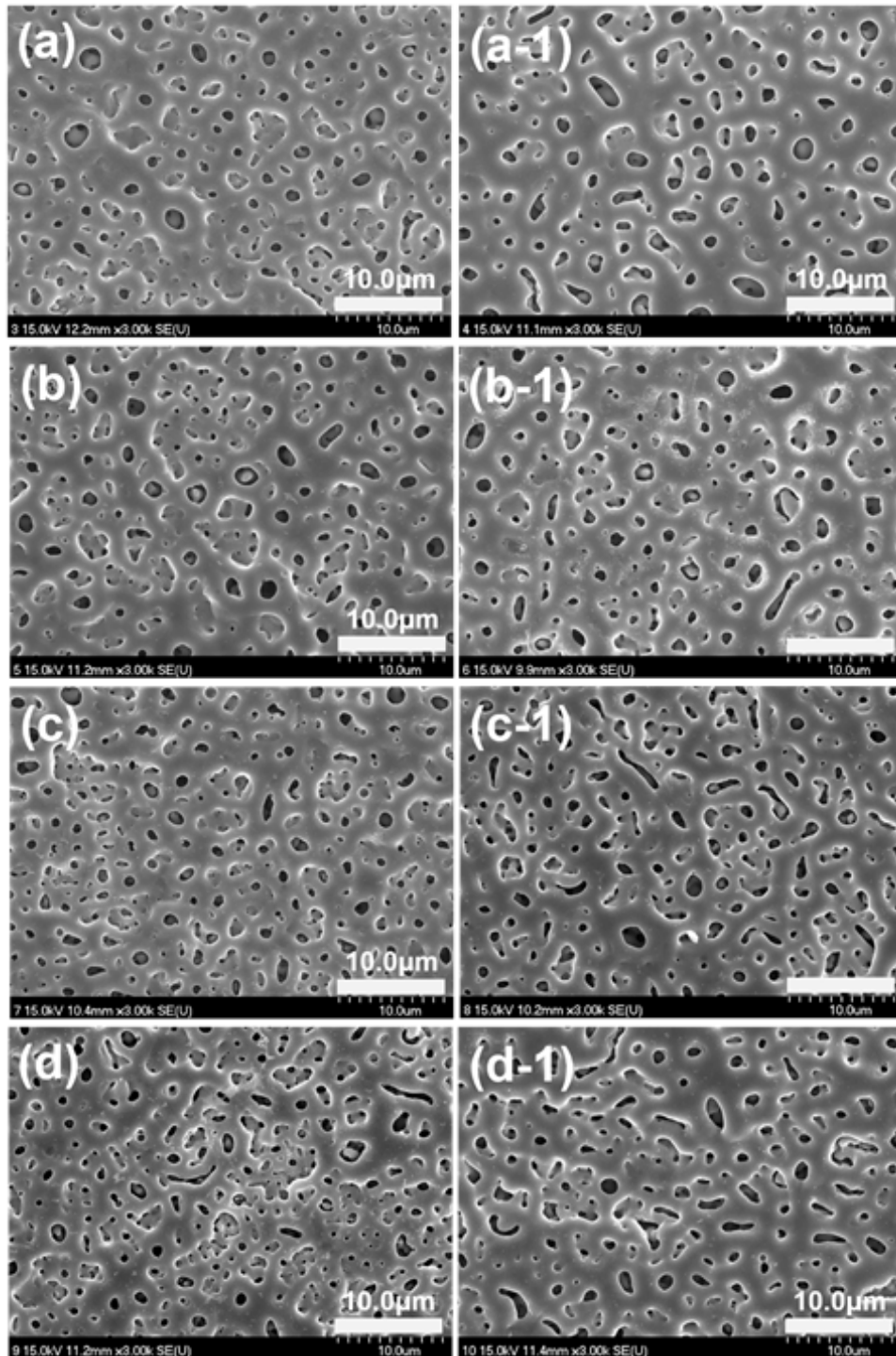


Fig. 15. FE-SEM images showing morphologies of PE0-treated Ti-29Nb alloy(a, b, c, and d) and Ti-29Nb-xHf alloy(a-1, b-1, c-1, and d-1) with different electrolytes containing Mg concentration of (a and a-1) 0 Mg (b and b-1) 5 Mg, (c and c-1) 10 Mg, and (d and d-1) 20 Mg.



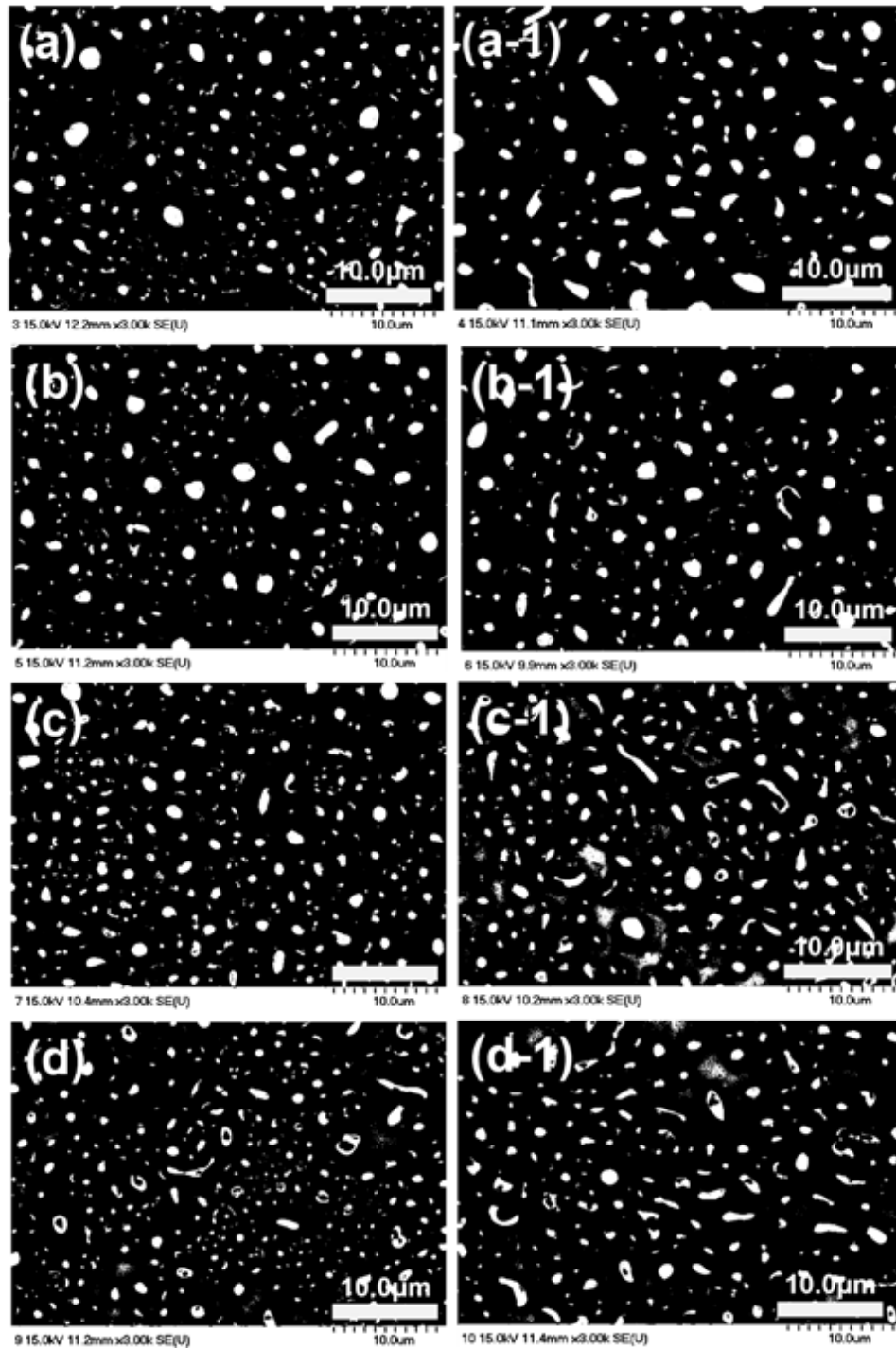


Fig. 16. FE-SEM and pore distribution images of micro-pore formed Ti-29Nb and Ti-29Nb-15Hf alloy by PEO processing with different electrolytes containing Mg concentration of (a and a-1) 0 Mg, (b and b-1) 5 Mg, (c and c-1) 10 Mg, and (d and d-1) 20 Mg.

Table 13. The summarized data from image analysis for the micro-pore formed on Ti-29Nb and Ti-29Nb-15Hf alloys by PE0.

	Numbers of micro-pore ( $N/10^2 \cdot \mu m^2$ )			
	(Ca+0Mg/P+5Si)	(Ca+5Mg/P+5Si)	(Ca+10Mg/P+5Si)	(Ca+20Mg/P+5Si)
Ti-29Nb	$22.98 \pm 1.77$	$31.35 \pm 1.75$	$54.33 \pm 1.34$	$59.45 \pm 0.15$
Ti-29Nb-15Hf	$23.43 \pm 2.11$	$31.66 \pm 2.32$	$55.67 \pm 1.54$	$60.77 \pm 0.23$
	Mean pore size ( $\mu m$ )			
	(Ca+0Mg/P+5Si)	(Ca+5Mg/P+5Si)	(Ca+10Mg/P+5Si)	(Ca+20Mg/P+5Si)
Ti-29Nb	$1.35 \pm 0.09$	$1.21 \pm 0.13$	$0.93 \pm 0.19$	$0.83 \pm 0.29$
Ti-29Nb-15Hf	$1.51 \pm 0.08$	$1.27 \pm 0.10$	$1.04 \pm 0.15$	$0.89 \pm 0.34$
	Area ratio of occupied by micro-pores ( $\%/10^2 \cdot \mu m^2$ )			
	(Ca+0Mg/P+5Si)	(Ca+5Mg/P+5Si)	(Ca+10Mg/P+5Si)	(Ca+20Mg/P+5Si)
Ti-29Nb	$10.59 \pm 0.33$	$11.02 \pm 0.47$	$12.17 \pm 0.55$	$13.15 \pm 0.32$
Ti-25Nb-15Hf	$9.83 \pm 0.29$	$10.99 \pm 0.44$	$12.38 \pm 0.51$	$13.11 \pm 0.41$

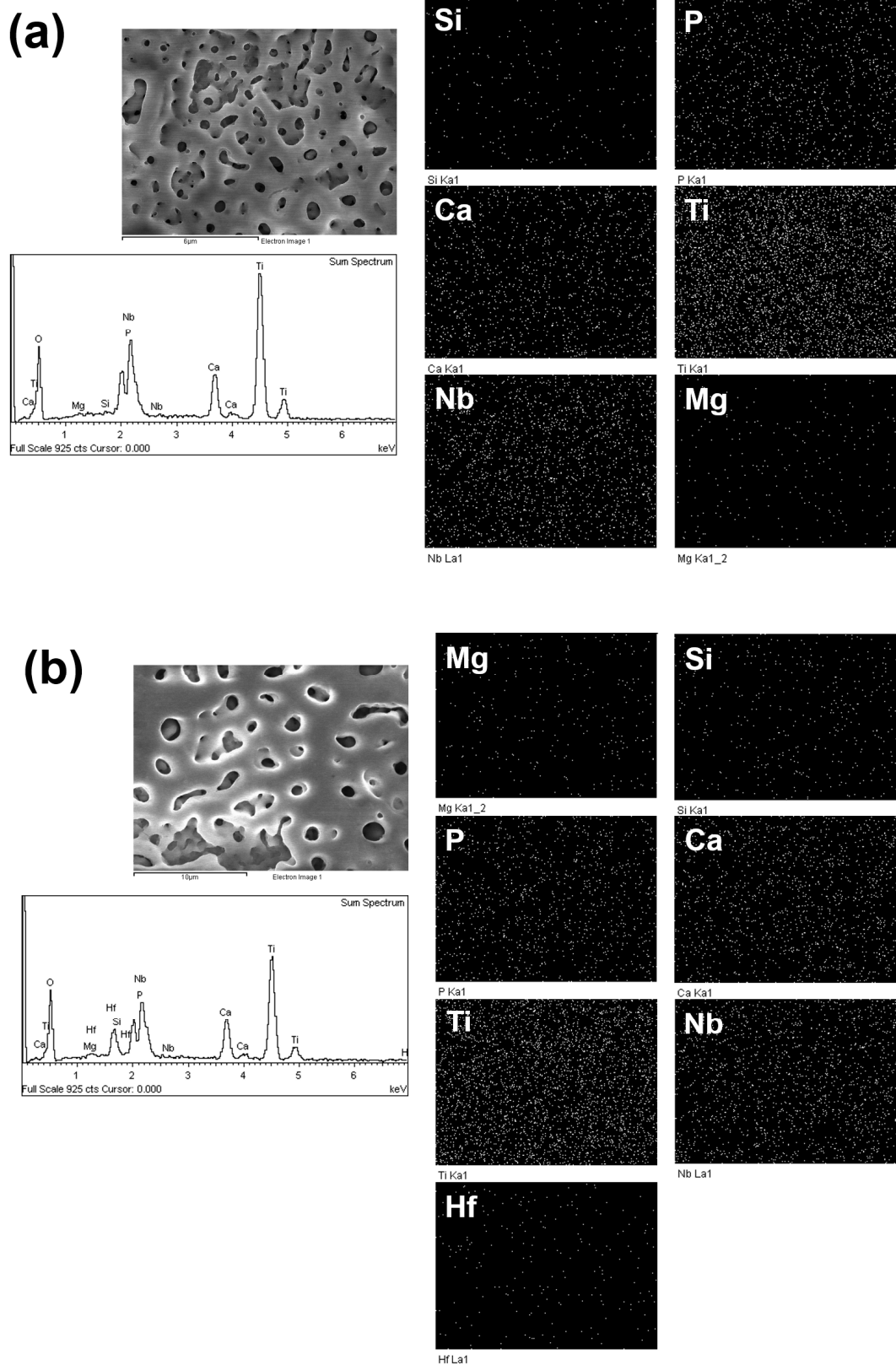


Fig. 17. EDS mapping analysis results of PEO-treated (a) Ti-29Nb and (b) Ti-29Nb-15Hf alloy.



Table 14. EDS mapping results of Ti-29Nb and Ti-29Nb-15Hf alloys with different electrolytes containing Mg concentration.

Samples	Composition (wt. %)									Ca/P	(Ca+xMg/P+5Si)
	O	Mg	Ca	Si	P	Ti	Hf	Nb	Total	ratio	ratio
<b>PEO 270-treated</b>											
Ti-29Nb (0Mg)	41.33	-	6.80	-	4.49	31.17	-	16.20	100.00	-	1.51
Ti-29Nb (5Mg)	36.29	0.14	11.30	0.50	6.52	36.29	-	11.14	100.00	1.73	1.62
Ti-29Nb (10Mg)	37.97	0.24	6.51	0.22	4.13	35.76	-	15.18	100.00	1.57	1.55
Ti-29Nb (20Mg)	38.58	0.47	6.60	0.22	4.46	35.28	-	14.39	100.00	1.47	1.51
<b>PEO 270-treated</b>											
Ti-29Nb-15Hf (0Mg)	36.32	-	6.08	-	4.20	33.29	9.27	10.84	100.00	-	1.44
Ti-29Nb-15Hf (5Mg)	38.40	0.09	6.99	0.30	4.00	28.98	7.01	14.53	100.00	1.74	1.64
Ti-29Nb-15Hf (10Mg)	35.17	0.40	6.03	0.31	4.14	31.48	8.93	13.55	100.00	1.45	1.44
Ti-29Nb-15Hf (20Mg)	38.77	0.82	5.69	0.11	4.61	31.16	4.10	14.74	100.00	1.23	1.38

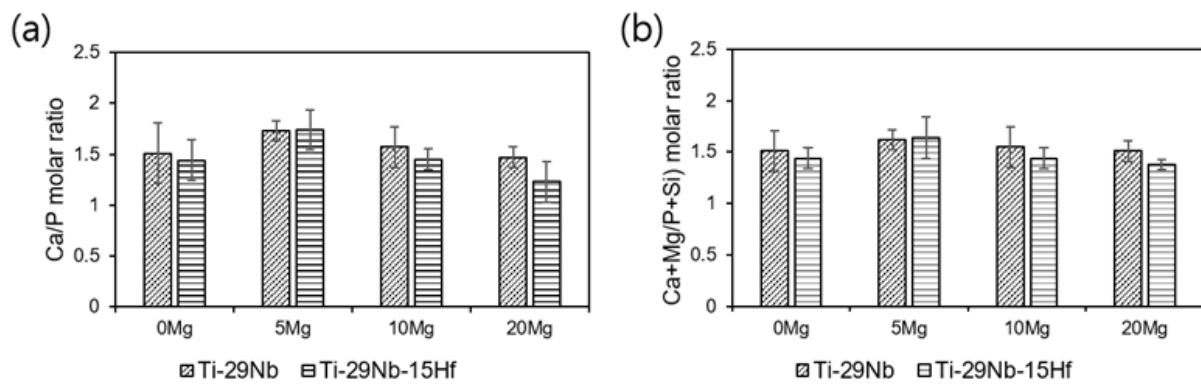


Fig. 18. Variation of Ca/P molar ratio with different electrolytes containing Mg concentration: (a) Ca/P ratio and (b) (Ca+Mg/P+Si) ratio.

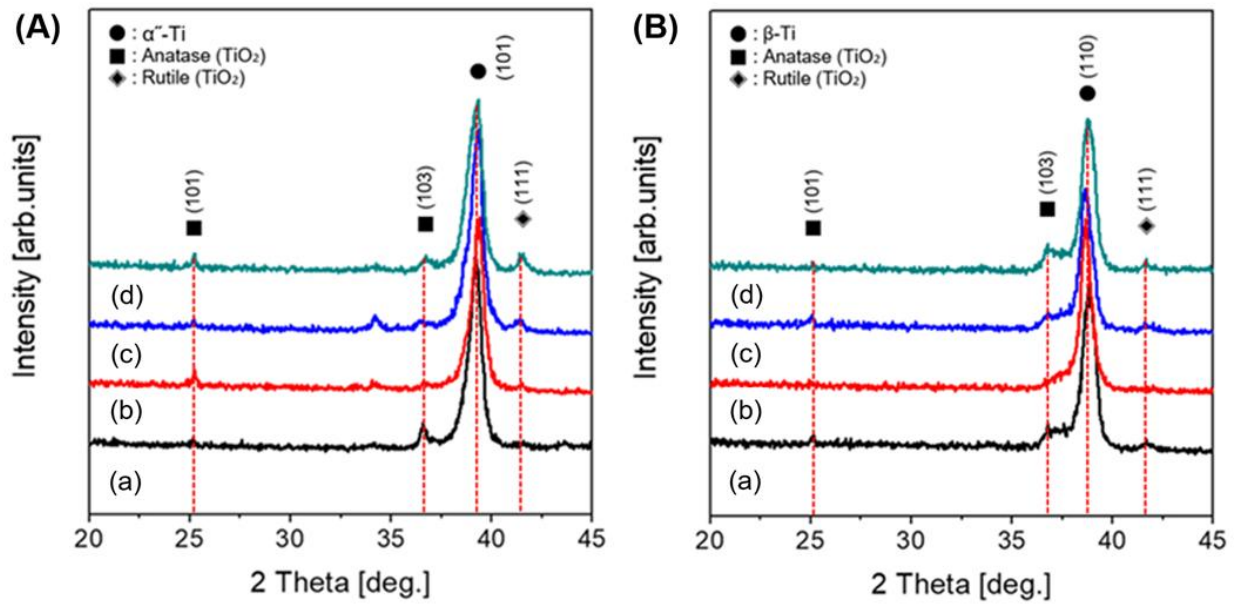


Fig. 19. TF-XRD patterns of PEO-treated Ti-29Nb and Ti-29Nb-15Hf alloys with different electrolytes containing Mg concentration: (a) 0 Mg, (b) 5 Mg, (c) 10 Mg, and (d) 20 Mg.

## 4.5. Electrochemical behaviors of Ti-29Nb and Ti-29Nb-15Hf alloys

Fig. 20 shows the anodic polarization curves of PEO treated Ti-29Nb-xHf alloys after potentiodynamic test in 0.9% NaCl solution at  $36.5 \pm 1^\circ\text{C}$ . Fig. 20(a) is Ti-29Nb and (b) is Ti-29Nb-15Hf, respectively. These values were obtained from the polarization curves and the Tafel curves using the negative and positive polarity branches of the curves, respectively. This phenomenon means the more higher corrosion resistance of PEO-treated Ti-29Nb-15Hf alloy compared to PEO-treated Ti-29Nb alloy. It can be seen that the corrosion potential of the PEO-treated Ti-29Nb-15Hf alloy are higher than that for the PEO-treated Ti-29Nb alloy. The value of  $E_{\text{corr}}$  for the PEO-treated Ti-29Nb alloy with Ca, P ions was -950 mV, while the corresponding values for the 0 Mg, 5Mg, 10Mg, and 20 Mg coatings were -920 mV, -880 mV, and -860 mV, respectively. And the value of  $E_{\text{corr}}$  for the PEO-treated Ti-29Nb-15Hf alloy with Ca, P ions was -850, -750, -720, and -660, respectively. The  $I_{\text{corr}}$  values of PEO-coated specimen were obtained from the polarization curves using Tafel line analysis. Furthermore, the decreases of corrosion current density in the bulk Ti alloy, relative to the  $I_{\text{corr}}$  value calculated for the other specimens, could be associated with an increase in the corrosion resistance of the dense oxid films such as  $\text{TiO}_2$ . The value of  $I_{\text{corr}}$  for the PEO-treated Ti-29Nb alloy was  $1.37 \times 10^{-6} \text{ A} \cdot \text{cm}^{-2}$ , while the corresponding values for the 0 Mg, 5 Mg, 10 Mg, and 20 Mg coatings were  $1.42 \times 10^{-6} \text{ A} \cdot \text{cm}^{-2}$ ,  $1.48 \times 10^{-6} \text{ A} \cdot \text{cm}^{-2}$ ,  $1.60 \times 10^{-6} \text{ A} \cdot \text{cm}^{-2}$ , respectively. The value of  $I_{\text{corr}}$  for the PEO-treated Ti-29Nb-15Hf alloy was  $1.77 \times 10^{-6} \text{ A} \cdot \text{cm}^{-2}$ , while the corresponding values for the 0 Mg, 5 Mg, 10 Mg, and 20 Mg coatings were  $9.76 \times 10^{-7} \text{ A} \cdot \text{cm}^{-2}$ ,  $9.63 \times 10^{-7} \text{ A} \cdot \text{cm}^{-2}$ ,  $1.03 \times 10^{-6} \text{ A} \cdot \text{cm}^{-2}$ , respectively.  $E_{\text{corr}}$  of PEO-treated Ti-29Nb-15Hf alloy with Mg concentration showed higher than that of PEO-treated Ti-29Nb alloy with Mg concentration. When the porous oxide layer is formed on the surface of the

specimen, it affects the thickness of the oxide film and increases OCP. Therefore, this reaction was able to obtain lower results in current density of PEO-coated specimen than current density in bulk specimen. In other words, a stable passive film is formed in the passive region of all specimen, as shown in Fig 20. The results for corrosion potential ( $E_{corr}$ ), corrosion current density ( $i_{corr}$ ), corrosion current density of oral environment at 300 mV ( $i_{300mV}$ ), current density of primary passivation( $i_{pp}$ ), and critical current density in passive region( $i_p$ ) from the polarization curves are given to Table 16. Especially, corrosion potential of PEO-treat Ti-29Nb-15Hf alloy with Mg concentration, that of  $E_{corr}$  increased compared to non-coated surface with Mg concentration. Also, the corrosion rate of the micro-pore formed Ti-29Nb and Ti-29Nb-15Hf alloy in solution containing Mg ions, decreased compared to the non-Mg treated surface. that of the micro-pore formed Ti-29Nb-15Hf alloy was lower than the corrosion rate of the micro-pore formed Ti-29Nb alloy. It is confirmed that the pore size and the number of the Ti-Nb alloy containing Hf element increased as compared with other samples. Although the titanium surface forms a stable passive film in the anodizing process, the active reaction in the pores can be affected by the corrosive solution. And surface pores tend to act as corrosion sites in NaCl solution [65-68].

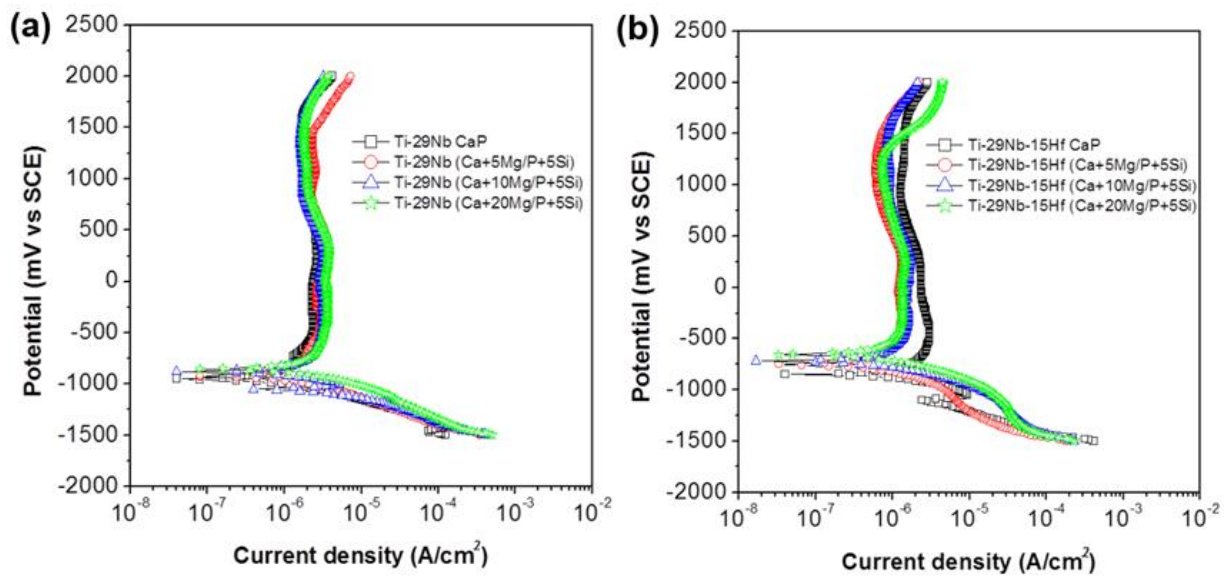


Fig. 20. Anodic polarization curves of PE0-treated Ti-29Nb-xHf alloys after potentiodynamic test in 0.9% NaCl solution at  $36.5 \pm 1^\circ\text{C}$ : (a) Ti-29Nb and (b) Ti-29Nb-15Hf.

Table 15. Electrochemical parameters of PEO-treated Ti-29Nb and Ti-29Nb-15Hf alloys with concentration of Mg ion from anodic polarization curves: corrosion potential( $E_{corr}$ ), corrosion current density( $i_{corr}$ ), current density at 300 mV( $i_{300mV}$ ), and primary passivation current density( $i_{pp}$ ).

Samples		$E_{corr}$ (mV)	$i_{300mV}$ ( $\mu A/cm^2$ )	$i_{corr}$ ( $\mu A/cm^2$ )	$i_{pp}$ ( $\mu A/cm^2$ )	$i_p$ ( $\mu A/cm^2$ )
Ti-29Nb	0Mg	-950	$2.63 \times 10^{-6}$	$1.37 \times 10^{-6}$	$1.56 \times 10^{-6}$	$1.42 \times 10^{-6}$
	5Mg	-920	$3.61 \times 10^{-6}$	$1.42 \times 10^{-6}$	$2.72 \times 10^{-6}$	$2.07 \times 10^{-6}$
	10Mg	-880	$3.21 \times 10^{-6}$	$1.48 \times 10^{-6}$	$2.80 \times 10^{-6}$	$1.42 \times 10^{-6}$
	20Mg	-860	$3.79 \times 10^{-6}$	$1.60 \times 10^{-6}$	$2.96 \times 10^{-6}$	$1.65 \times 10^{-6}$
Ti-29Nb-15Hf	0Mg	-850	$2.80 \times 10^{-6}$	$1.77 \times 10^{-6}$	$2.84 \times 10^{-6}$	$1.16 \times 10^{-6}$
	5Mg	-750	$1.29 \times 10^{-6}$	$9.76 \times 10^{-7}$	$1.27 \times 10^{-6}$	$5.43 \times 10^{-7}$
	10Mg	-720	$1.67 \times 10^{-6}$	$9.63 \times 10^{-7}$	$1.42 \times 10^{-6}$	$7.36 \times 10^{-7}$
	20Mg	-660	$1.42 \times 10^{-6}$	$1.03 \times 10^{-6}$	$1.30 \times 10^{-6}$	$6.32 \times 10^{-7}$

## 4.6. Biocompatibility of Ti-29Nb and Ti-29Nb-15Hf alloys

Fig. 21 shows the contact angle measurements of Ti-29Nb and Ti-29Nb-15Hf surfaces with different electrolytes containing Mg concentration of (a and a-1) 0 Mg, (b and b-1) 5 Mg, (c and c-1) 10 Mg, and (d and d-1) 20 Mg, respectively. In Fig. 24 (a), (b), (c), and (d) of PEO-treated Ti-29Nb alloy, the contact angles are  $48.71^\circ$ ,  $45.09^\circ$ ,  $41.58^\circ$ , and  $39.53^\circ$ , respectively. And in Fig. 21 (a-1), (b-1), (c-1), and (d-1), the contact angles are  $49.11^\circ$ ,  $38.81^\circ$ ,  $37.10^\circ$ , and  $36.64^\circ$ , respectively. From the Fig. 21, the contact angles of PEO-treated Ti-29Nb and Ti-29Nb-15Hf alloys in different electrolytes containing Mg ion shows slightly the lower value compared with PEO treated Ti-29Nb and Ti-29Nb-15Hf alloys in electrolytes un-containing Mg ions. Porosity was formed on the PEO-treated surface, and as the Hf content increased, the pore size decreased and secondary pore was formed in the first formed pore. Such a high wettability leads to a good biocompatibility for the implant surface [69-72]. Also, surface morphology of micro-pore structure is important to achieve improved cell adhesion on Ti alloy implant surfaces. Therefore, micro-pore formed oxide surface of Ti alloys shows a hydrophilic behavior, due to complete spreading of water on the entire and into the pores. It is thought that, the surface roughness is an important factor in the contact angle of the implant surface, and the implant surface should have a low contact angle and high surface roughness in order to be suitable for the living body [69-75].

Fig. 22 FE-SEM images showing morphology of bone-like apatite formed Ti-29Nb-15Hf alloy, (a) low-magnification ( $\times 5,000$ ) and (b) high-magnification ( $\times 50,000$ ), respectively. Fig. 22 (a)-(b) indicate bone-like apatite formed well in the SBF for every specimen. The bone-like apatite of the PEO-treated Ti-29Nb-15Hf alloy surface was formed definitively in the hole. It is thought that apatite formation in the hole can help to fix the implant [72-76].



Fig. 23 shows the FE-SEM images morphology of bone-like apatite formed Ti-29Nb and Ti-29Nb-15Hf alloys with Mg concentration after anodization at 270 V for 3min. Fig. 23 (a) is 0 Mg, (b) is 5 Mg, (c) is 10 Mg, and (d) is 20 Mg for Ti-29Nb micro-pore surface, and Fig. 23 (a-1) is 0 Mg, Fig. 23 (b-1) is 5 Mg, Fig. 23 (c-1) is 10 Mg, and Fig. 23 (d-1) is 20 Mg, respectively. From the bone-like apatite formed results, bone-like apatite is well formed on the surface of 5 Mg/Si PEO-treated Ti-29Nb-15Hf alloy compared to the other specimen after SBF immersion. Generally, these reactions are thought to be influenced by the action of Mg and Si ions in the human body. It is known that Mg and Si ions are closely related to tissue calcification in the human body and indirectly affect mineral metabolism [77].

Fig. 24 shows the FE-SEM images showing morphology of cell cultured Ti-29Nb-15Hf, (a) is low-magnification (x 1,000), middle-magnification (x 3,000), and (b) is high-magnification (x 10,000). Fig. 24 shows the cell growth of PEO-treated Ti-29Nb-15Hf alloy with Mg concentration at 37 °C for 1day. The mouse osteoblastic cell line MC3T3-E1(DSMZ, Braunschweig, Germany) was used in cell culture. The pores and surfaces were well covered with lamellipodia and filopodia on the PEO-treated Ti-29Nb-15Hf alloy in the solution containing Ca, P, Mg, and Si ions. In Fig. 24, cell growth on the surface can be observed. Cell was proliferated from the nucleus to micro-pore formed surface.

Fig. 25 shows the FE-SEM images showing morphology of cell cultured Ti-29Nb and Ti-29Nb-15Hf alloys for 1day. Fig. 25 (a) is 0 Mg, Fig. 25 (b) is 5 Mg, Fig. 25 (c) is 10 Mg, and Fig. 25 (d) is 20 Mg for Ti-29Nb, and Ti-29Nb, Fig. 25 (a-1) is 0 Mg, Fig. 25 (b-1) is 5 Mg, Fig. 25 (c-1) is 10 Mg, and Fig. 25 (d-1) is 20 Mg, respectively. In the case of PEO-treated Ti-29Nb and Ti-29Nb-15Hf alloy with Mg concentration, the number and growth of cells were distributed all pore surface. Cell culture and high wettability are closely related, and surface morphology of micro-pore formed alloy is important to achieve improved cell adhesion. According to previous study,

According to previous study, Mg is the most abundant cation in the human body as a factor that induces the proliferation of osteoblasts. Therefore, magnesium plays an active role in the process of new bone tissue formation process [75-80].

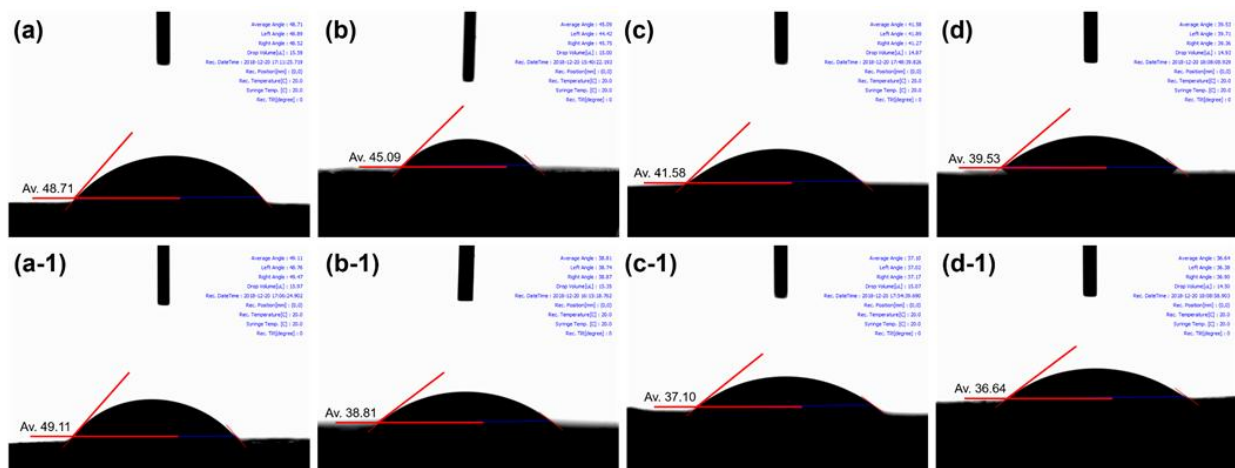


Fig. 21. Contact angles measurements of Ti-29Nb and Ti-29Nb-15Hf alloy surfaces: (a and a-1) 0 Mg, (b and b-1) 5 Mg, (c and c-1) 10 Mg, and (d and d-1) 20 Mg.

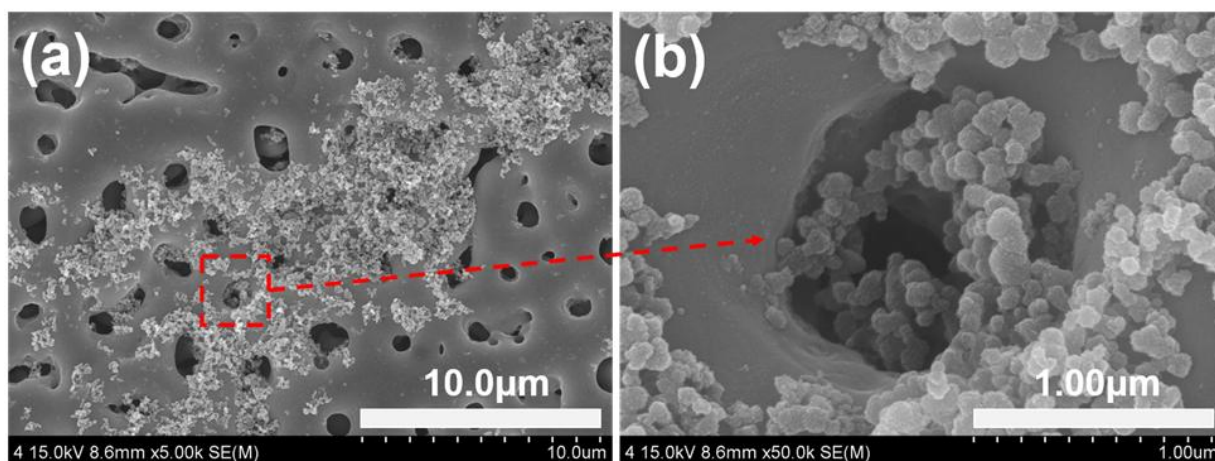


Fig. 22. FE-SEM images showing morphology of bone-like apatite formed Ti-29Nb-15Hf alloy: (a) low-magnification (x 5,000) and (b) high-magnification (x 50,000).

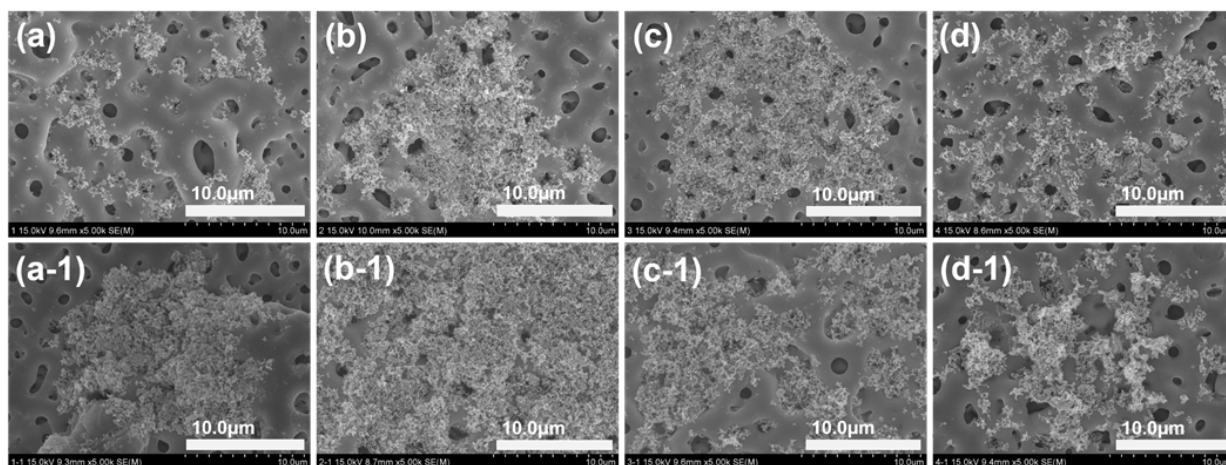


Fig. 23. FE-SEM images showing morphology of bone-like apatite: Ti-29Nb alloy: (a) 0 Mg, (b) 5 Mg, (c) 10 Mg, and (d) 20 Mg, and Ti-29Nb-15Hf alloy: (a-1) 0 Mg, (b-1) 5 Mg, (c-1) 10 Mg, and (d-1) 20 Mg.

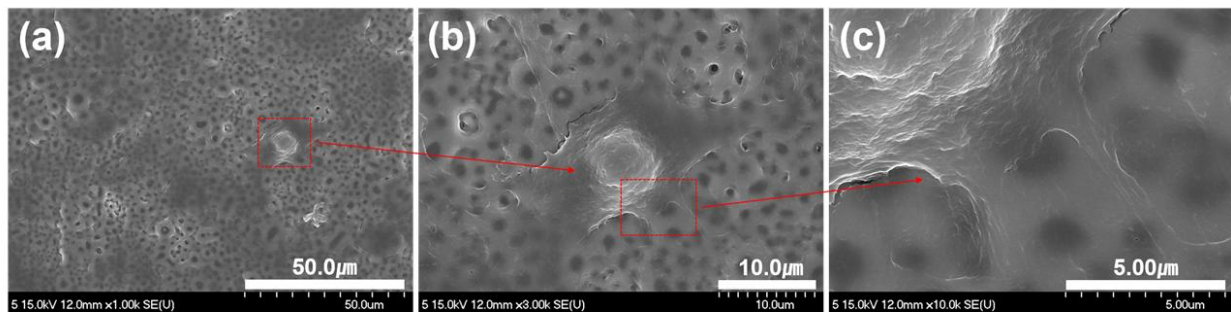


Fig. 24. FE-SEM images showing morphology of cell cultured Ti-29Nb-15Hf alloy: (a) low-magnification (x 1,000), middle-magnification (x 3,000), and (b) high-magnification (x 10,000).

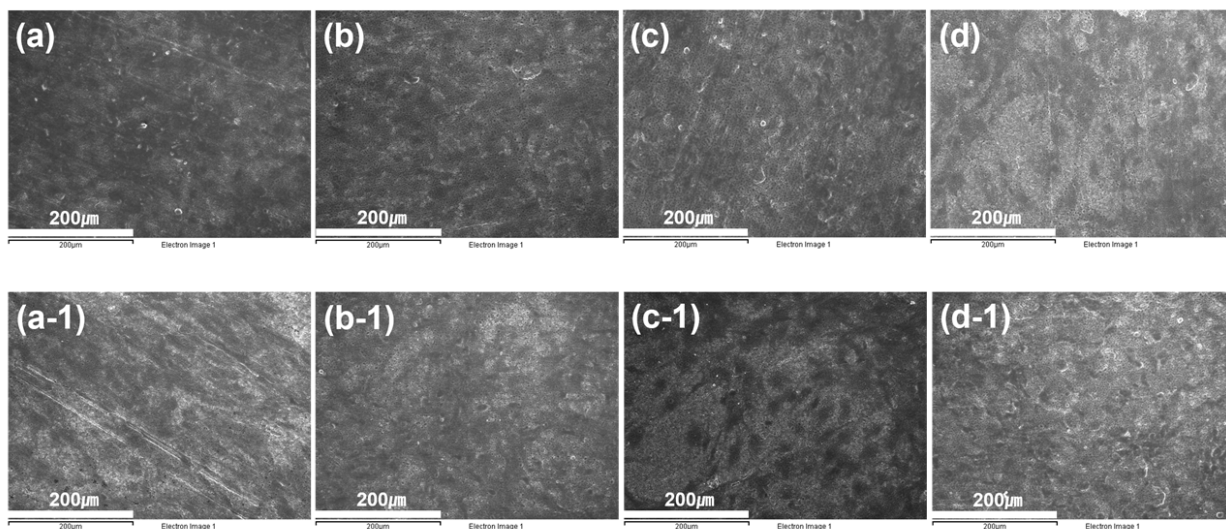


Fig. 25. FE-SEM images showing morphology of cell cultured Ti-29Nb-xHf alloys for 1day: Ti-29Nb alloy: (a) 0 Mg, (b) 5 Mg, (c) 10 Mg, and (d) 20 Mg, and Ti-29Nb-15Hf alloy: (a-1) 0 Mg, (b-1) 5 Mg, (c-1) 10 Mg, and (d-1) 20 Mg.



## V. CONCLUSIONS

In this study, surface characteristics of PEO-treated Ti-29Nb-xHf alloy in electrolytes containing Ca, P, Mg, and Si ions have been researched. The results were as follows;

1. The microstructure of the Ti-29Nb-xHf alloys showed  $\alpha'$  and  $\beta$  phase. As the Hf content increased, the shape of the needle-like decreased and the shape of the equiaxed structure and the  $\beta$  phase increased.
2. The hardness of Ti-29Nb-xHf alloy decreased slightly as the Hf content increased, and elastic modulus decreased.
3. The surface of oxide films showed the uniform micro-pore formation on the surface. Especially, in the case of PEO-treated Ti-29Nb-xHf alloys in electrolytes containing Mg ion, pore size decreased and numbers increased compared to PEO-treated Ti-29Nb-xHf alloys in electrolytes without Mg ion.
4. From the XRD analysis, in the case of Mg ion addition to electrolyte, the anatase peak on the Ti-29Nb-xHf alloy was shifted slightly to left side with a lower diffraction angle,
5. The Ca/P and (Ca+Mg)/(Si+P) ratios were the closest to the ideal value for PEO-treated Ti-29Nb and Ti-29Nb-15Hf in solution containing 5Mg Mol%. Also, these ratios of PEO-treated Ti-29Nb-xHf alloys in solution containing Mg and Si ions decreased as Mg ion increased.
6. Corrosion potential of the PEO-treated Ti-29Nb-xHf alloys increased as Mg ion increased, and corrosion potential of PEO-treated Ti-29Nb-15Hf alloy showed higher than that of the Ti-29Nb alloy.
7. The contact angles of micro-pore formed Ti-29Nb and Ti-29Nb-15Hf alloy surface with Mg ions showed lower than those of other alloy surface.



8. The PEO-treated Ti-29Nb-15Hf alloy in electrolytes containing 5Mol Mg was a good cell proliferation and growth with lamellipodia and filopodia covered the pores and surfaces.

In conclusion, the formation of the anatase and micro-pore on Ti-29Nb-xHf alloys can be controlled by varying the Mg concentration of electrolyte for improvement of biocompatibility.

## Reference

1. C. X. Wang, M. Wang, X. Zhou, Nucleation and growth of apatite on chemically treated titanium alloy: an electrochemical impedance spectroscopy study, *Biomaterials* 24 (2003) 3069.
2. S. Stojadinovic, N. Tadic, R. Vasilic, Formation and characterization of ZnO films on zinc substrate by plasma electrolytic oxidation, *Surf. Coat. Technol.* 307 (2016) 650.
3. M. Niinomi, D. Kuroda, K. Fukunaga, M. Morinaga, Y. Kato, T. Yashiro, A. Suzuki, Corrosion wear fracture of new  $\beta$  type biomedical titanium alloys, *Mat. Sci. Eng. A.* 263 (1999) 193.
4. Y. Okazaki, Y. Ito, A. Ito, T. Tateishi, Effect of alloying elements on mechanical properties of titanium alloys for medical implants, *J. Inst. Metals.* 34 (1993) 1217.
5. C. Chenglin, Z. Jingchuan, Y. Zhongda, L. Pinghua. Optimal design and fabrication of hydroxyapatite-Ti asymmetrical functionally graded biomaterial. *Mater Sci Eng A* 348 (2003) 244.
6. M. Niinomi, Fatigue performance and cyto-toxicity of low rigidity titanium alloy, Ti-29Nb-13Ta-4.6Zr, *Biomaterials* 24 (2003) 2673.
7. V. S. Saji, H. C. Choe, and W. A. Brantely, An electrochemical study on self-ordered nanoporous and nanotubular oxide on Ti-35Nb-5Ta-7Zr alloy for biomedical applications, *Acta Biomater.* 5 (2009) 2303.
8. S. Y. Park, H. C. Choe, Effects of Hf content on nanotubular structure of Ti-29Nb-xHf ternary alloys, *Surf. Coat. Technol.* 320 (2017) 109.
9. E. Boanini, M. Gazzano, A. Bigi, Ionic substitutions in calcium phosphates synthesized at low temperature, *Acta. Biomater.* 6 (2010) 1882.
10. Y. L. Zhou, M. Niinomi, T. Akahori, Changes in mechanical properties of Ti alloys in relation to alloying additions of Ta and Hf, *Mater. Sci. Eng. A* 483 (2008) 153.

11. Z. Cai, M. Koike, H. Sato, M. Brezner, Q. Guo, M. Komatsu, O. Okuno, T. Okabe, Electrochemical characterization of cast Ti-Hf binary alloys, *Acta Biomater.* 1 (2005) 353.
12. D. Krupa, J. Baszkiewica, J.A. Kozibowski, Barcz A, J.W. Sobzak, A. Bilinski, M.D. Lewandowska-Szumiel, B. Rajchel, Effect of calcium-ion implantation on the corrosion resistance and biocompatibility of titanium, *Biomaterials* 22 (2001) 2139.
13. R. Boyer, G. Welsch, E. W. Collings, *Materials properties handbook: titanium alloys*, ASM, Metals Park, Ohio. (1993) 483.
14. M.C. Andrade, M.S. Sader, M.R.T. Filgueiras, T. Orasawara, Microstructure of ceramic coating on titanium surface as a result of hydrothermal treatment, *J. Mater. Sci- Mater. Med* 11 (2000) 751.
15. D. A. Hanaor, C. C. Sorrell, Review of the anatase to rutile phase transformation, *J. Mater. Sci.* 46 (2011) 855.
16. A. I. Chun, J. G. Morales, H. Fenniri, T. J. Webster, Helical rosette nanotubes: a more effective orthopaedic implant material, *Nanotechnology* 15 (2004) 234.
17. L. Xuanyong, K. C. Paul, D. Chuanxian, Surface modification of titanium, titanium alloys, and related materials for biomedical application, *Mater, Sci.Eng. R* 47 (2004) 49.
18. I. J. Hwang, H. C. Choe, W. A. Brantley, Electrochemical characteristics of Ti-6Al-4V after plasma electrolytic oxidation in solution containing Ca, P, and Zn ions, *Surf. Coat. Technol.* 320 (2017) 458.
19. E. Bertoni, A. Bigi, G. Cojazzi, M. Gandolfi, S. Panzavolta, N. Roveri, Nanocrystals of magnesium and fluoride substituted hydroxyapatite, *J. Inorg. Biochem.* 72 (1998) 29.
20. S. J. Kalita, H. A. Bhatt, Nanocrystalline hydroxyapatite doped with magnesium and zinc: Synthesis and characterization, *Mater. Sci. Eng. C* 27 (2007) 837.
21. B. D. Ratner, A. S. Hoffman, F. J. Schoen, J. E. Lemons, *Biomaterials science: an introduction to materials in medicine*, Academic Press, New

- York (1996).
22. J. B. Park, Biomaterials science and engineering, Plenum Press, New York (1984).
  23. B. O. Aronsson, J. Lausmaa, B. Kasemo, Glow discharge plasma treatment for surface cleaning and modification of metallic biomaterials, J. Biomed. Mater. Res. 35 (1997) 49.
  24. H. C. Choe, W. G. Kim, Y. H. Jeong, Surface characteristics of HA coated Ti-30Ta-xZr and Ti-30Nb-xZr alloys after nanotube formation, Surf. Coat. Technol. 205 (2010) 305.
  25. B. D. Ratner, A. S. Hoffman, F. J. Sheon, J. E. Lemons, Biomaterials Science: an introduction to materials in medicine, Elsevier Academic Press, San Diego, CA, ed. 2 (2004) 556.
  26. S. Onder, F. N. Kok, K. Kazmanli, M. Urgan, Magnesium substituted hydroxyapatite formation on (Ti,Mg)N coatings produced by cathodic arc PVD technique, Mater Sci Eng C. 33 (2013) 4337.
  27. M. McCrachen, Dental implant materials: Commercially pure titanium and titanium alloy, J. Prosthodont. 8 (1999) 40.
  28. S. C. Cox, P. Jamshidi, L. M. Grover, K. K. Mallick, Preparation and characterisation of nanophase Sr, Mg, and Zn substituted hydroxyapatite by aqueous precipitation, Mater. Sci. Eng. C 35 (2014) 106.
  29. J. J. Kim, I.S. Byeon, W. A. Brantley, H. C. Choe, Highly ordered nanotubular film formation on Ti-25Nb-xZr and Ti-25Ta-xHf, Thin Solid Films 596 (2015) 94.
  30. E. W. Collings, Applied superconductivity, metallurgy, and physics of titanium alloys, vol. 1 and 2, Plenum Press, New York (1986).
  31. R. Boyer, G. Welsch, E. W. Collings, ASM international, Metals Park, Ohio (1994).
  32. S. B. Maslennikov, E. A. Maslennikova, Steels and alloys at high temperatures, Metallurgy Press, Moscow (1991) 465.
  33. C. Chenglin, Z. Jingchuan, Y. Zhongda, L. Pinghua, Optimal design and fabrication of hydroxyapatite-Ti asymmetrical functionally graded

- biomaterial, *Mater Sci Eng A* 348 (2003) 244.
34. A.L. Yerokhin, X. Nie, A. Leyland, A. Matthews, S.J. Dowey, Plasma electrolysis for surface engineering, *Surf. Coat. Technol.* 122 (1999) 73.
  35. W. G. Kim, H. C. Choe, W. A. Brantley, Nanostructured surface changes of Ti-35Ta-xZr alloys with changes in anodization factors, *Thin Solid Films* 519 (2011) 4663.
  36. V. Aina, L. Bergandi, G. Lusvardi, G. Malavasi, F. E. Imrie, I. R. Gibson, G. Cerrato, D. Ghigo, Sr-containing hydroxyapatite: morphologies of HA crystals and bioactivity on osteoblast cells, *Mater Sci Eng C* 33 (2013) 1132.
  37. S. Horiuchi, M. Hiasa, A. Yasue, K. Sekine, K. Hamada, K. Asaoka, E. Tanaka, Fabrications of zinc-releasing biocement combining zinc calcium phosphate to calcium phosphate cement, *J. Mech. Behav. Bioed. Mater.* 29 (2014) 151.
  38. T. Huang, Y. Xiao, S. Wang, Y. Huang, X.Liu, F. Wu, Z. Gu, Nanostructured Si, Mg,  $\text{CO}_3^{2-}$  substituted hydroxyapatite coatings deposited by liquid precursor plasma spraying: synthesis and characterization, *J. Therm. Spray Technol.* 20 (2011) 829.
  39. D.M. Brunette, P. Tengvall, M. Textor, P. Thomsen, *Titanium in medicine*, Springer, Berlin (2001) 485.
  40. R. Van Noort, *Titanium: The implant material of today*, *J. Mater. Sci.* 22 (1987) 3801.
  41. D. Buser, T. Nydegger, T. Oxlad, D.L. Cochran, R.K. Schenk, H.P. Hirt, D. Snetivy, L.P. Nolte, Interface shear strength of titanium implants with a sandblasted and acid-etched surface: A biomechanical study in the maxilla of miniature pigs, *J. Biomed. Mater. Res.* 45 (1999) 75.
  42. S. Y. Park, H. C. Choe, Variations of nanotubes on the Ti-Nb-Hf alloys with applied voltages, *Thin Solid Films* 620 (2016).
  43. M. Kononen, M. Hormia, J. Kivilahti, J. Hautaniemi, I. Thesleff, Effect of surface processing on the attachment, orientation, and proliferation of human gingival fibroblasts on titanium, *J. Biomed. Mater. Res.* 26

- (1992) 1325.
44. I.J. Hwang, H.C. Choe, W. A. Brantley, Electrochemical characteristics of Ti-6Al-4V after plasma electrolytic oxidation in solutions containing Ca, P, and Zn ions, *Surf. Coat. Technol.* 320 (2017) 458.
  45. Z. Schwartz, J.Y. Martin, D.D. Dean, J. Simpson, D.L. Cochran, B.D. Boyan, Effect of titanium surface roughness on chondrocyte proliferation, matrix production, and differentiation depends on the state of cell maturation, *J. Biomed. Mater. Res.* 30 (1996) 145.
  46. H. M. Kim, F. Miyaji, T. Kokubo, T. Nakamura, Preparation of bioactive Ti and its alloys via simple chemical surface treatment, *J. Biomed. Mater. Res.* 32 (1996) 409.
  47. J. M. Yu, H. C. Choe, Mg-containing hydroxyapatite coatings on Ti-6Al-4V alloy for dental materials, *Appl. Surf. Sci.* 432 (2018) 294.
  48. P. Kurze, W. Krysmann, H.G. Schneider, Application fields of ANOF layers and composites, *Cryst. Res. Technol.* 21 (1986) 1603.
  49. H. Ahn, D. Lee, K.M. Lee, K. Lee, D. Baek, S.W. Park, Oxidation behavior and corrosion resistance of Ti-10Ta-10Nb alloy, *Surf & Coat Tech* 202 (2008) 5784.
  50. A. L. Yerokhin, X. Nie, A. Leyland, A. Matthews, S. J. Dowey, Plasma electrolysis for surface engineering, *Surf. Coat. Technol.* 122 (1999) 73.
  51. E. Boanini, M. Gazzano, A. Bigi, Ionic substitutions in calcium phosphates synthesized at low temperature, *Acta Biomater.* 6 (2010) 1882.
  52. G. R. Fischer, P. Bardhan, J. E. Geiger, The lattice thermal expansion of hydroxyapatite, *J. Mater. Sci. Lett.* 2 (1983) 577.
  53. M. P. Moreira, G. D. de Almeida Soares, J. Dentzer, K. Anselme, L. A. de Sena, A. Kuznetsov, E. A. dos Santos, Synthesis of magnesium and manganese-doped hydroxyapatite structures assisted by the simultaneous incorporation of strontium, *Mater. Sci. Eng. C* 61 (2016) 736.
  54. E. Boanini, M. Gazzano, A. Bigi, Ionic substitutions in calcium phosphates synthesized at low temperature, *Acta. Biomater.* 6 (2010) 1882.
  55. L. Yang, S. Perez-Amodio, Y.F. Florence, B.D. Groot, V. Everts, CAV.

- Blitterswijk, P. Habibovic, The effects of inorganic additives to calcium phosphate on in vitro behavior of osteoblasts and osteoclasts, *Biomaterials* 31 (2010) 2976.
56. M. Sato, M.A. Sambito, A. Aslani, N.M. Kalkhoran, E.B. Slamovich, T.J. Webster, Increased osteoblast functions on undoped and yttrium-doped nanocrystalline hydroxyapatite coatings on titanium, *Biomaterials* 27 (2006) 2358.
57. W. Xue, H.L. Hosick, A. Bandyopadhyay, S. Bose, C. Ding, K.D.K. Luk, K.M.C. Cheung, W.W. Lu, Preparation and cell-materials interactions of plasma sprayed strontium-containing hydroxyapatite coating, *Surf. Coat. Technol.* 201 (2007) 4685.
58. W. Xue, K. Dahlquist, A. Banerjee, A. Bandyopadhyay, S. Bose, Synthesis and characterization of tricalcium phosphate with Zn and Mg based dopants, *J. Mater. Sci. Mater. Med.* 19 (2008) 2669.
59. A. Bandyopadhyay, S. Bernard, W. Xue, S. Bose, Calcium phosphate-based resorbable ceramics: influence of MgO, ZnO, and SiO<sub>2</sub> dopants, *J. Am. Ceram. Soc.* 89 (2006) 2675.
60. S. Y. Park, C. I. Jo, H. C. Choe, Hydroxyapatite deposition on micropore-formed Ti-Ta-Nb alloys by plasma electrolytic oxidation for dental applications, *Surf. Coat. Technol.* 294 (2016) 15.
61. C. Chu, J. Zhu, Z. Yin, P. Lin, Optimal design and fabrication of hydroxyapatite-Ti asymmetrical functionally graded biomaterial, *Mater. Sci. Eng. A* 348 (2003) 244.
62. X. Li, Y. Sogo, A. Ito, H. Mutsuzaki, N. Ochiai, T. Kobayashi, The optimum zinc content in set calcium phosphate cement for promoting bone formation in vivo, *Mater. Sci. Eng.* 29 (2009) 969.
63. G. Jin, H. Cao, Y. Qiao, F. Meng, H. Zhu, X. Liu, Ostrogenic activity and antibacterial effect of Zinc ion implanted titanium, *Colloids and Surfaces B: Biointerfaces* 117 (2014) 158.
64. X. Yang, S. Yu, Wen. Li, Preparation of bioceramic films containing hydroxyapatites on Ti-6Al-4V alloy surfaces by the micro-arc oxidation

- technique, Mater. Res. Bull. 44 (2009), 947.
65. S. Y. Park, H. C. Choe, Mn-coatings on the micro-pore formed Ti-29Nb-xHf alloys by RF-magnetron sputtering for dental applications, Appl. Surf. Sci. 432 (2009) 278.
  66. Y. L. Zhou, M. Niinomi, T. Akahori, M. Nakai, H. Fukui, Comparison of various properties between titanium-tantalum alloy and pure titanium for biomedical applications, Materials Transactions 48 (2007) 380.
  67. S. Durdu, O. F. Deniz, I. Kutbay, M. Usta, Characterization and formation of hydroxyapatite on Ti6Al4V coated by plasma electrolytic oxidation, J. Alloys Compd. 551 (2013) 422.
  68. F. Ren, Y. Leng, R. Xin, X. Ge, Synthesis, characterization and ab initio simulation of magnesium-substituted hydroxyapatite, Acta Biomater. 6 (2010) 2787.
  69. S. R. Kim, J. H. Lee, Y. T. Kim, D. H. Riu, S. J. Jung, Y. J. Lee, S. C. Chung, Y. H. Kim, Synthesis of Si, Mg substituted hydroxyapatites and their sintering behaviors, Biomaterials 24 (2003) 1389.
  70. E. Landi, A. Tampieri, M. Mattioli-Belmonte, G. Celotti, M. Sandri, A. Gigante, P. Fava, G. Biagini, Biomimetic Mg- and Mg<sub>2</sub>CO<sub>3</sub>-substituted hydroxyapatites: synthesis characterization and in vitro behaviour, J. Eur. Ceram. Soc. 26 (2006) 2593.
  71. Y Cui, R Xu and D. Li(1997). Experimental studies of the  $\omega$  phase in a titanium alloy, in Japan-China Workshop on Titanium Alloys and Intermetallics, NRM 111.
  72. S. Y. Park, H. C. Choe, Electrochemical characteristics of nanotubular Ti-25Nb-xZr ternary alloys for dental implant materials, J. Nanosci. Nanotechnol. 18 (2018) 2.
  73. Y Murakami(1980). Critical Review Phase Transformation and Heat Treatment, in Titanium 80 Science and Technology, Metallurgical Society of AIME 158.
  74. S. Y. Park, H. C. Choe, Manganese coatings on hydroxyapatite-deposited Ti-29Nb-xHf alloys after nanomesh formation, J. Nanosci. Nanotechnol. 17



- (2017) 4.
75. J. H. Schemel, ASTM manual on zirconium and hafnium, ASTM Int. (1977) 1.
  76. J. J. Kim, I. S. Byeon, W. A. Brantley, H. C. Choe, Highly ordered nanotubular film formation on Ti-25Nb-xZr and Ti-25Ta-xHf, Thin Solid Films 596 (2015) 94.
  77. U. Brägger, W. Bürgin, N. P. Lang, D. Buser, Digital subtraction radiography for the assessment of changes in peri-implant bone density, International Journal of Oral & Maxillofacial Implants 6 (1991) 160.
  78. Z. Schwartz, C. H. Lohmann, J. Oefinger, L. F. Bonewald, D. D. Dean, B. D. Boyan, Implant surface characteristics modulate differentiation behavior of cells in the osteoblastic lineage, Advances in dental research 13 (1999) 38.
  79. D. M. Brunette, B. Chehroudi, The effects of the surface topography of micromachined titanium substrata on cell behavior in vitro and in vivo, J. Biomech. Eng. 121 (1999) 49.
  80. C. Capuccini, P. Torricelli, F. Sima, E. Boanini, C. Ristoscu, B. Bracci, G. Socol, M. Fini, I. N. Mihailescu, A. Bigi, Strontium-substituted hydroxyapatite coatings synthesized by pulsed-laser deposition: In vitro osteoblast and osteoclast response, Acta Biomater. 4 (2008) 1885.

## 저작물 이용 허락서

학 과	치의학과	학 번	20147446	과 정	박사
성 명	한글: 박 선 영    한문: 朴 宣 映    영문: PARK SEON YEONG				
주 소	광주광산구 장덕동 신안실크밸리 106동 801호				
연락처	E-MAIL : seonyeong2840@hanmail.net				
논문제목	한글 : 플라즈마 전해 산화법으로 (Mg, Si)-hydroxyapatite 코팅된 치과 임플란트용 Ti-29Nb-xHf 합금의 표면 특성 영어 : Surface characteristics of (Mg/Si)-hydroxyapatite coated Ti-29Nb-xHf alloys by plasma electrolyte oxidation for dental implant				

본인이 저작한 위의 저작물에 대하여 다음과 같은 조건아래 조선대학교가 저작물을 이용할 수 있도록 허락하고 동의합니다.

- 다 음 -

1. 저작물의 DB구축 및 인터넷을 포함한 정보통신망에의 공개를 위한 저작물의 복제, 기억장치에의 저장, 전송 등을 허락함
2. 위의 목적을 위하여 필요한 범위 내에서의 편집·형식상의 변경을 허락함.  
다만, 저작물의 내용변경은 금지함.
3. 배포·전송된 저작물의 영리적 목적을 위한 복제, 저장, 전송 등은 금지함.
4. 저작물에 대한 이용기간은 5년으로 하고, 기간종료 3개월 이내에 별도의 의사 표시가 없을 경우에는 저작물의 이용기간을 계속 연장함.
5. 해당 저작물의 저작권을 타인에게 양도하거나 또는 출판을 허락을 하였을 경우에는 1개월 이내에 대학에 이를 통보함.
6. 조선대학교는 저작물의 이용허락 이후 해당 저작물로 인하여 발생하는 타인에 의한 권리 침해에 대하여 일체의 법적 책임을 지지 않음
7. 소속대학의 협정기관에 저작물의 제공 및 인터넷 등 정보통신망을 이용한 저작물의 전송·출력을 허락함.

동의여부 : 동의(    )    반대( √ )

2019 년    08 월    23 일

저작자:                      박선영                      (서명 또는 인)

**조선대학교 총장 귀하**